

CATALYST DEVELOPMENT FOR THE REFORMING OF LIQUID HYDROCARBONS

Christina R. Manns, Bret H. Howard, and Charles E. Taylor

U.S. Department of Energy
National Energy Technology Laboratory
P.O. Box 10940
Pittsburgh, PA 15236-0940

Introduction

Fuel cells are rapidly being recognized as an alternative source of electricity to power automobiles, light-duty trucks and in small stationary applications. Fuel cells, powered by hydrogen, have the potential to be the cleanest and most efficient source of electricity for use by the automotive industry. The goal of this project is to develop a process that utilizes a liquid hydrocarbon fuel as the hydrogen source for an on-board fuel cell. One of the major problems in current reforming processes is the byproduct carbon monoxide (CO). CO is a poison to the proton exchange membrane (PEM) fuel cell catalyst which is platinum based [1,2].

The objective of this research is to reduce the quantity of CO produced during hydrocarbon reforming to near-zero levels under mild reforming conditions. To accomplish this, two major topics must be examined: the composition of the catalyst and the type of liquid hydrocarbon that is being reformed. Currently, methanol is favored as the chemical carrier for hydrogen for fuel cell applications. Methanol can be produced from a variety of fossil fuels and has a high energy density. Since it is a liquid, methanol is more easily adaptable to the existing fuel infrastructure, requiring similar transportation and storage facilities as those already in use.

Ideally, a reforming catalyst would have hydrocarbon feed flexibility or the ability to effectively reform a variety of hydrocarbon feeds. However, this is not easily accomplished at the moderate temperatures (330-400°C) at which the catalyst must operate. The desired products would be hydrogen and carbon dioxide, with no production of CO. Most conventional reforming processes operate at higher temperatures, producing a significant quantity of CO. Also, higher operating temperatures are not cost effective due to increased energy consumption and more stringent materials requirements.

Copper-based catalysts are known to have potential for reforming applications, and were selected for this study. Previous studies have indicated that these catalysts are active for steam reforming at temperatures that are low enough to minimize the production of CO and that these catalysts are stable under the target operating conditions [3,4]. Steam reforming employs the water-gas shift (WGS) reaction maximizing production of H₂ with negligible production of CO.

The purpose of this study is to develop stable, copper-based catalysts capable of reforming methanol at moderate temperatures to produce H₂ and CO₂ with little or no CO or other byproduct yield. This study examined neat methanol feeds as well as methanol/water feeds (1:1 volume) as the reactants in the reforming process. Results are compared to studies reported in the literature that used either water and methanol or water and ethanol as reactants at molar ratios of 1.0 or 1.3.

Experimental

Several techniques were employed in the catalyst preparations. These techniques included sequential precipitation, co-precipitation with sequential precipitation, and incipient wetness impregnation. Generally, nitrate salts of the metals were used to prepare catalyst precursors at carefully controlled pH. Precursors were washed, dried

at 120°C overnight followed by calcination in air at 350°C for 6 hours.

For both the freshly prepared and used catalysts, the following were determined: the surface area was determined by the Brunauer, Emmett, and Teller (BET) method, the composition was examined by Inductively Coupled Plasma-Atomic Emission Spectroscopy (ICP-AES), and the morphology was determined by scanning-electron microscopy (SEM).

All reforming reactions were conducted in a 0.5-inch O.D. x 0.375-inch I.D. (1.27 cm O.D. x 0.95 cm I.D.) x 10-inch (25.4 cm) 304 stainless steel reactor. The inside wall of the reactor was coated with Silcosteel® (Restek) coating. The catalyst was supported in the reactor between quartz-wool plugs and the reactor was operated in an up-flow configuration. A gold-plated thermocouple in the center of the catalyst bed was used to monitor the temperature of reaction to $\pm 0.5^\circ\text{C}$. Proportional ratio mass-flow controllers (Brooks) were used to feed the gases to the reactor. A high-pressure syringe pump (Isco) controlled feeds of liquids to the reactor. The feeds were preheated to approximately 130°C prior to entering the reactor and the products of reaction were held at approximately 150°C between the exit of the reactor and the cold trap, which was maintained at -4°C .

Reaction conditions were as follows: 1 gram (± 0.001) of catalyst was placed in the reactor supported between deactivated-quartz wool plugs. A gold-plated thermocouple was placed in the middle of the catalyst bed. The reactor was purged with helium at 5 mL/min for at least 2 hours. The temperature of the reactor was increased to either 150°C or 255°C. Methanol flow was started at a weight hourly space velocity of 1 hr^{-1} after the catalyst had reached the target temperature.

Products of reaction were directly sampled and analyzed by an online dual-column gas chromatograph (GC). The GC (Hewlett-Packard 5890 Series II) was equipped with a 6 ft x 0.125 O.D. 80/100 Porapak Q and a 20 ft x 0.125 O.D. 60/80 Molecular Sieve 5Å (both obtained from Supelco). The GC was operated at a constant temperature of 100°C during elution. Argon was used as the carrier gas having an average linear velocity at 30°C of 30 mL/min for the Molecular Sieve column and 50 mL/min for the Porapak Q column. The Molecular sieve column was used to separate the light gaseous products while the Porapak Q column was used to identify unreacted liquid hydrocarbons. Both columns were equipped with back-flushing capability. Dual thermal conductivity detectors (TCDs) were employed to detect the separated components.

Results and Discussion

Reforming of methanol was done using methanol only and also using methanol and water with a 1:1 volume basis. Reforming of methanol only was run at various reaction temperatures. **Table I** lists the data from a series of methanol-reforming reactions.

TABLE I. Results of Methanol Reforming Reactions

Catalyst	Temp. (°C)	CH ₃ OH Conversion (%)	H ₂ (%)	CO ₂ (%)	CO (%)
Cu/Zn/Zr/Al/Y*	150	21.2	8.9	91.1	0.0
Cu/Zn/Zr/Al/Y*	255	72.2	91.1	8.9	0.0
Cu/Zn/Zr/Al/Y**	255	49.1	77.6	16.6	5.8
Cu/Zn/Ce/on γ -Al ₂ O ₃	255	85.1	47.2	22.5	29.3
Cu/Zr/ on γ -Al ₂ O ₃	255	80.9	53.5	40.6	5.9
Cu/Zn/Zr/ on γ -Al ₂ O ₃	255	90.5	45.5	35.2	19.3

* 69/17/10/2/2 mole percent ** 8/2/64/13/13 mole percent

Table I shows that methanol conversion increases with reaction temperature. For the Cu/Zn/Zr/Al/Y (69/17/10/2/2 mole %) catalyst at 150°C, methanol conversion was approximately 21%. The

majority of product detected by the GC was carbon dioxide. When the reaction temperature was increased to 255°C, conversion of methanol increased initially to 80%. The product selectivity also increased, with hydrogen comprising 91% of the product stream.

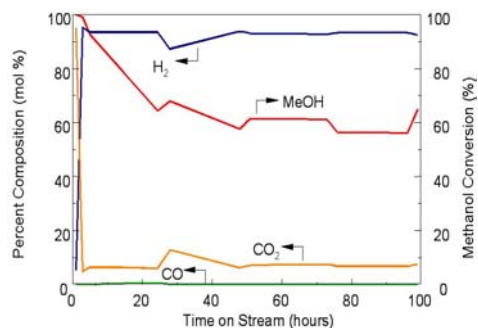


Figure 1. Results of methanol conversion over Cu/Zn/Zr/Al/Y catalyst as a function of time.

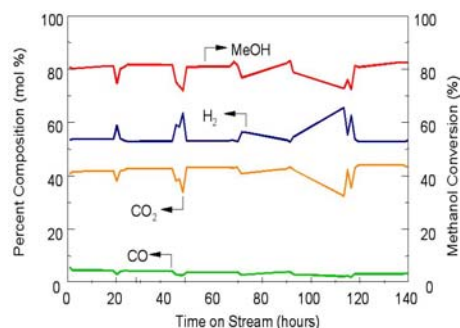


Figure 2. Results of methanol conversion over Cu/Zr on γ -Al₂O₃ catalyst as a function of time.

Figure 1 shows an extended conversion run for the Cu/Zn/Zr/Al/Y (69/17/10/2/2 mole percent) catalyst. Methanol conversion decreased with time on stream at 255°C. This decrease is due to coke formation during the reaction. The results for this catalyst were similar to those reported in the literature [3]. Conversion of methanol was low at 150°C and increased with increasing temperature. Conversions of methanol at 250°C were greater than 50% in both cases. Differences arise when the product slate is examined. This catalyst produced larger quantities of carbon dioxide than reported for the literature catalyst. Of importance is that carbon monoxide was not detected at either reaction temperature in our investigation or in the literature [3] with the Cu/Zn/Zr/Al/Y catalyst.

Figure 2 shows an extended conversion run for the Cu/Zr on γ -Al₂O₃ (7/3/90 mole %) catalyst. As is shown in **Figure 2**, conversion of methanol at 255°C is relatively stable with time on stream as are the products produced. This catalyst did exhibit CO production at 255°C, however coking was much less than that observed with the Cu/Zn/Zr/Al/Y catalyst.

The same group of catalysts was run using a 1:1 volume methanol/water feed and a reaction temperature of 250°C. The results of the reactions of methanol and water are listed in Table II. As shown in **Table II**, conversion of methanol for all the catalysts, except for the Cu/Zn/Zr/Al/Y, which had a very low surface area, were greater than 99%. Experiments using co-fed water with methanol exhibited lower carbon monoxide product levels than experiments run with methanol alone, as would be expected. Table two also shows that when using methanol and water as a co-feed at 250°C, methanol conversions increased by an additional 50%.

TABLE II. Results of Methanol/Water Reforming Reactions

Catalyst	Temp. (°C)	CH ₃ OH Conversion (%)	H ₂ (%)	CO ₂ (%)	CO (%)
Cu/Zn/Zr/Al/Y*	250	100	59.0	35.8	4.3
Cu/Zn/Zr/Al/Y**	250	21.2	7.9	4.8	0.0
Cu/Zn/Ce/on γ -Al ₂ O ₃	250	99.0	57.6	38.5	3.7
Cu/Zr/ on γ -Al ₂ O ₃	250	99.4	43.2	30.4	1.1
Cu/Zn/Zr/ on γ -Al ₂ O ₃	250	99.7	60.9	38.0	0.98

* 69/17/10/2/2 mole percent ** 8/2/64/13/13 mole percent

Figure 3 shows an extended conversion run for a 1:1 methanol/water reaction over the Cu/Zn/Zr/ on γ -Al₂O₃ (12/2.5/2.5/83 mole %) catalyst. As shown in **Figure 3**, conversion of methanol at 255°C remains constant with time on stream. It should be noted that carbon monoxide was negligible at either reaction temperature in this investigation with the Cu/Zn/Zr/ on γ -Al₂O₃ catalyst.

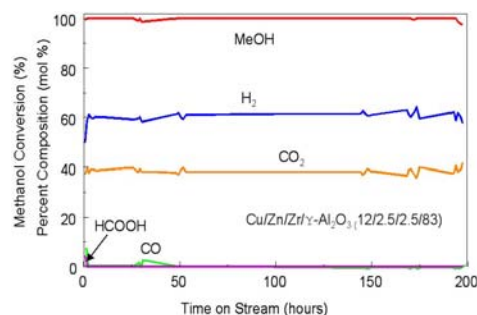


Figure 3. Results of methanol/water conversion over Cu/Zn/Zr on γ -Al₂O₃ catalyst as a function of time.

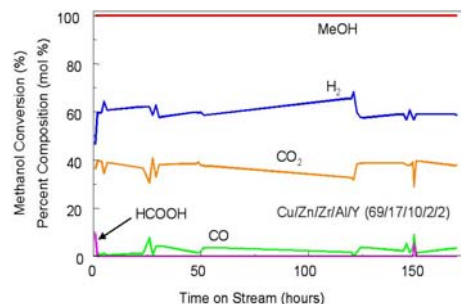


Figure 4. Results of methanol/water conversion over Cu/Zn/Zr/Al/Y catalyst as a function of time.

Figure 4 shows an extended conversion run for a 1:1 methanol/water reaction over the Cu/Zn/Zr/Al/Y (69/17/10/2/2 mole %) catalyst. As shown in **Figure 4**, conversion of methanol at 255°C is relatively stable with time on stream as are the reaction products. This catalyst did exhibit CO production at 255°C; however, coking was not observed.

Table III. Catalyst Surface Area

Catalyst Composition (mole %)	Surface Area (as prepared) (m ² /g)	Surface Area (after reaction) (m ² /g)	Surface Area (after reaction with H ₂ O) (m ² /g)
Cu/Zn/Zr/Al/Y 69/17/10/2/2	92	55	57
Cu/Zn/Zr/Al/Y 8/2/64/13/13	21	16	54
Cu/Zr on γ -Al ₂ O ₃ 12/5/83	200	188	193
Cu/Zn/Zr on γ -Al ₂ O ₃ 12/2.5/2.5/83	198	187	186
Cu/Zn/Ce on γ -Al ₂ O ₃ 12/2.5/2.5/83	194	195	194

Table III shows the surface area of the catalyst as prepared, after 150 hours of reaction with methanol reforming and after 150 hours of methanol/water reforming. Both catalyst preparations of Cu/Zn/Zr/Al/Y exhibit a loss of surface area after reaction probably due to coking. The three catalysts supported on γ -Al₂O₃ retain more than 90% of the prepared surface area. These catalysts were also the most stable of all the catalysts tested.

In summary, reforming results with neat methanol show higher methanol conversions than those reported in the literature, also using neat methanol, over an extended period of time. Yields of H₂, CO₂, and CO for reforming of neat methanol are comparable to those reported in the literature for reforming of water: methanol mixtures at similar molar ratios [3].

Using methanol with water (1:1 volume) as a feed resulted in higher methanol conversions and slightly higher hydrogen yields than experiments using neat methanol. The methanol:water feed also produced higher hydrogen yields when compared to methanol:water reforming yields reported in the literature [3]. After reviewing the results, a Cu/Zn/Zr catalyst on γ -Al₂O₃ was selected for further testing using other liquid hydrocarbons. This catalyst was selected because it produced the lowest amount of CO during extended methanol:water reforming runs while maintaining high conversion and product yields. Preliminary experimental runs using this catalyst with neat ethanol and ethanol with water (1:1 volume) have been completed. The results show that the production of CO is slightly less with neat ethanol than the methanol:water, while CO production is reduced another 50% in the ethanol:water reforming reaction over neat ethanol only. Preliminary results show that direct reforming of coal derived liquid hydrocarbons with a pre-determined amount of water may remain a low-cost option for on-board production of hydrogen.

Conclusions

Several catalysts have been synthesized that are capable of reforming methanol at moderate temperatures. The main products of reaction using water with either methanol or ethanol are hydrogen and carbon dioxide. A higher selectivity for H₂ was observed for the catalysts prepared for this study although some coking was observed under certain reactor conditions. However, when the WGS reaction was employed, a decrease in CO production resulted. A direct correlation between the catalyst's surface area, methanol and ethanol conversion, and catalyst stability is observed.

Acknowledgement

The authors would like to acknowledge the technical assistance of Richard R. Anderson, Heather A. Elsen, Edward P. Ladner, and Dirk D. Link.

Disclaimer

Reference in this report to any specific commercial product, process, or service is to facilitate understanding and does not necessarily imply its endorsement or favoring by the United States Department of Energy.

References

1. Borroni-Bird, C.E. *Journal of Power Sources* **1996**, 61, 33-48.
2. National Renewable Energy Laboratory report, DOE/GO-10095-088, DE94011827, February 1995.
3. Breen, J.P. and Ross, J.R.H. *Catalysis Today* **1999**, 51, 521.
4. S. Velu, K. Suzuki, M.P. Kapoor, T. Osaki, And F. Ohashi *Journal of Catalysis* **2000**, 194, 373-384.
5. Taylor, C.E. and Manns, C.R. *Preprints of the Fuels Division* 2001, 46(2), 652.

SELECTIVE CO OXIDATION IN A HYDROGEN RICH STREAM OVER Au/MnO_x AND Au/FeO_x CATALYSTS

Dao T. *, Luengnaruemitchai A. *, Osuwan S. *, and Gulari E. **

*The Petroleum and Petrochemical College, Chulalongkorn University, Bangkok, Thailand

**Department of Chemical Engineering, University of Michigan, Ann Arbor, Michigan, USA

Introduction

Having a lot of good characteristics fuel cells have been becoming one of the most considerations in many applications especially in transportation. H₂ is the most suitable fuel for the fuel cell technology. However, because of the H₂ explosion risk and the limitation of H₂ onboard storage tank it requires integrating H₂ production unit with fuel cell unit. Steam reforming is an efficient, economical and widely-used process for H₂-production. Coming out with H₂ is a small amount of CO which poisons the Pt anodes reducing the overall fuel cell performance. Thus, in order to obtain the maximum performance, removal of CO from the reformed gas has been done.

There are several ways to remove CO from H₂-rich gas but selective oxidation of CO is the best choice. It has been found that supported-Au catalyst is one of the best candidates for selective CO oxidation. In comparison with Pt group metal catalysts, it is substantially more active for CO oxidation than H₂ oxidation resulting in the higher selectivity.¹ This paper focused on gold/manganese-oxide catalyst (Au/MnO_x) and gold/ferrous-oxide catalyst (Au/FeO_x).

Experimental

Preparation of Catalysts. Co-precipitation was used for catalyst preparation. An aqueous solution of 1 M Na₂CO₃ was added dropwise into an aqueous mixture of 0.1 M Mn(NO₃)₂ or 0.1 M Fe(NO₃)₃ and 0.1 M HAuCl₄ (Au/Mn or Au/Fe = 1/30 atomic ratio) under vigorous stirring condition at 80°C. The mixture was kept at a pH of 8 for 1 h. The precipitate was separated out from solution by centrifuge at 2,000 rpm for 5 min. Excess ions were eliminated by washing with warm deionized water. Deionized precipitate was dried at 110°C overnight and calcined at 300°C in case of Au/MnO_x and 400°C in case of Au/Fe₂O₃ for 2 h.

Activity Measurement. The catalytic activity measurements were carried out in the fixed bed reactor packed with 100 mg catalyst at 80-120 mesh in size. The feed gas contained 1% CO, 2% CO₂, 1% O₂, 2.6% H₂O and 40% H₂ balanced in He passing through the catalyst bed at the total flow rate of 50 ml/min (SV=30,000 mlg⁻¹h⁻¹) at atmospheric pressure. Prior to all experiments, He and O₂ pretreatments^{2,3} at 200°C for 2 h were needed for Au/MnO_x and Au/FeO_x, respectively. The effluent gas was detected by online gas chromatograph. For the water vapor effect, reactant gases were passed through a water bubbler.

Catalyst Characterization. The determination of surface area was done using the Autosorb-1 Gas Sorption System and analyzed by Autosorb Anygas Software Version 2.1. Crystallite structure of support and average particle diameter of gold were analyzed by the Rigaku X-Ray Diffractometer system with Cu tube for generating CuK_α radiation (1.5406 Å) and nickel filter. RINT-2200 was used to obtain XRD pattern at 40 kV and 30 mA. Scan speed of 5°/min with scan step of 0.02 was used for a continuous run in 5 to 90° range. Atomic Absorption Spectroscopy (AAS), VARIAN model 300/400 was utilized to determine the actual percent Au loading on the supports. Transmission Electron Microscope

(TEM) was carried out using a JEM 2010 operating at 200 kV in bright and dark field modes. Crystallinity and crystal structure of the sample were evaluated from selected area electron diffraction pattern.

Results and Discussion

Catalyst Characterization. Surface area, crystallite size and actual percent Au loading of two types of catalyst are shown in **Table 1**. High surface area of Au/FeO_x due to a well dispersed Au metal on support which is quite cleared by the crystallite size smaller than 3 nm in XRD results is shown in **Figure 1**. The percent Au loadings on both catalysts are about 5-6% which are relatively higher than Pt loading on conventional Pt supported catalyst.²

Table 1. Surface Area, Crystallite Size and Actual Percent Au Loading of Catalysts

Type of catalyst	Surface area (m ² /g)	Crystallite size (nm)	Au loading (%)
Au/MnO _x	118.90	14	5.70
Au/FeO _x	94.87	<3	5.38

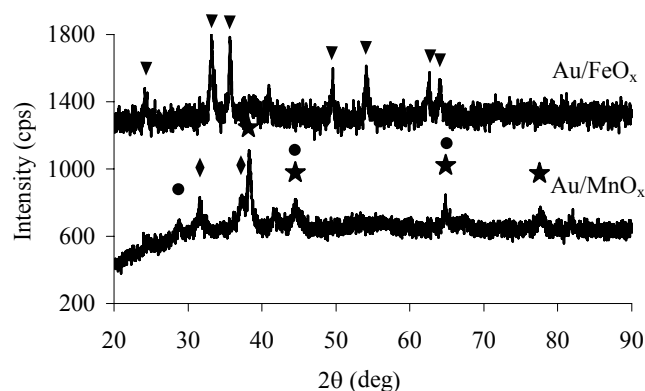


Figure 1. XRD patterns of prepared catalysts. ★ Au; ◆ MnCO₃; ● Mn₃O₄; ▼ Fe₂O₃.

No XRD peak of Au ($2\theta = 38.2^\circ$, 44.4° , 64.1° , and 78.0°) was observed in XRD pattern of Au/FeO_x indicating that Au crystallite size was smaller than 3 nm.

Figure 2 shows TEM images of both catalysts. MnO_x support seems like semi-crystal while FeO_x is highly crystallized. Au crystal structure was also investigated to be hemispherical in shape and that attached to the support by their flat planes.⁴ Average Au particle sizes were identical to the results from XRD.

Catalyst Activity. **Figure 3 and 4** show the conversion and selectivity of both catalysts as a function of temperature with the reactant gas mixture of 1%CO, 1%O₂, 2%CO₂, 2.6%H₂O, and 40% H₂ balanced in He. The selectivity of both catalysts were maximum at low temperature and then slightly decreased with increasing temperature reflecting a higher apparent activation energy for H₂ oxidation than for CO oxidation. Maximum conversion of Au/MnO_x was approximate 95% with 60% selectivity at the relatively low temperature of 130°C. For Au/FeO_x, the activity was readily reached 100% at 50°C and then slightly decreased to 90% at 90°C. The selectivity was around 50% at this temperature.

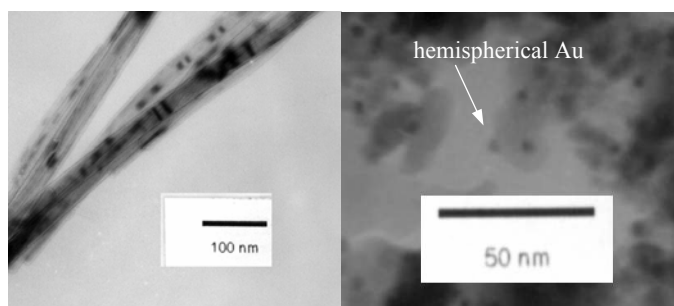


Figure 2. TEM images of Au/MnO_x and Au/FeO_x.

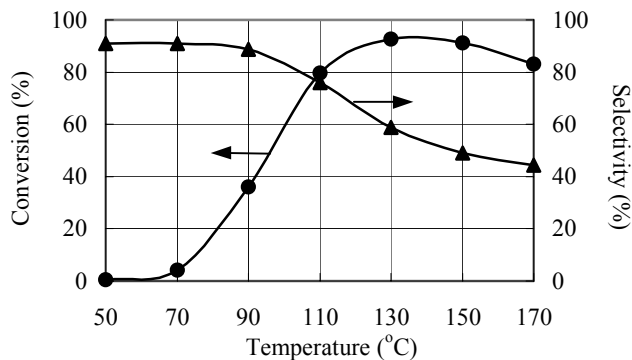


Figure 3. Activity of Au/MnO_x versus temperature.

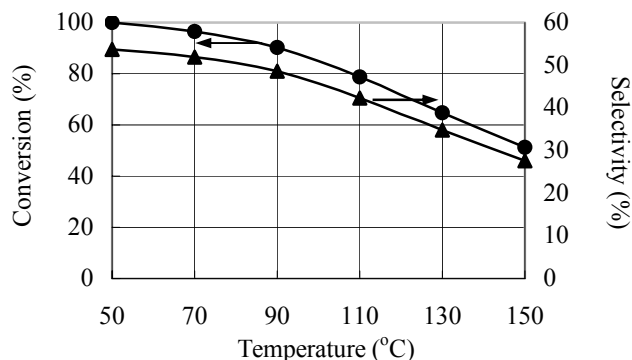


Figure 4. Activity of Au/FeO_x versus temperature.

In comparison with Pt/ γ -Al₂O₃, a commonly used catalyst requires relatively high operating temperature of 200°C, Au/MnO_x and Au/FeO_x were superior not only in term of their appropriate working temperature but also by high activities. Although the amount of Au needed for these kinds of catalyst were higher than Pt/ γ -Al₂O₃, it is still preferred because of the shortage of Pt when it is utilized as electrodes for fuel cells.

Effect of CO₂. The effect of the presence of CO₂ in the feed stream on the catalytic behavior of both catalysts is shown in **Figure 5**. Increasing from 2 to 6%, CO₂ lowered the maximum conversion of Au/MnO_x and Au/FeO_x about 4 and 3%, respectively. It seems that CO₂ caused the detrimental effect on the catalyst activity because of the CO₂ retention on the catalyst surface.³ However, this effect became slightly small at the operating temperature.

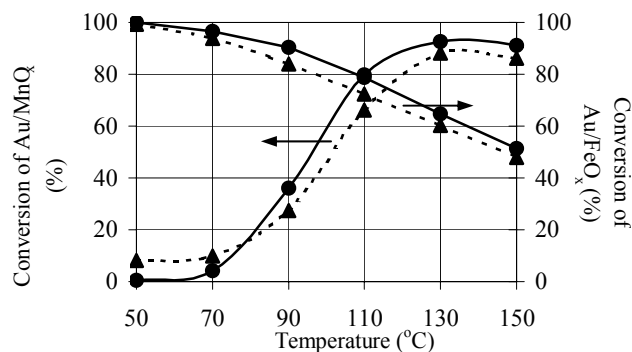


Figure 5. Effect of CO₂ on the activity of both catalysts. Solid lines, 2%CO₂; dotted lines, 6%CO₂.

Effect of Water. Generally, the catalytic activity of catalyst is depressed in the presence of water. **Figure 6** shows the effect of water vapor in the reaction gas mixture on the conversion of catalysts. Under the unhumidified condition, the catalyst activities were less active. Water seemed to be favorable to the catalyst activity^{2,5} since it provided hydroxyl group which is necessary for reaction to take place.

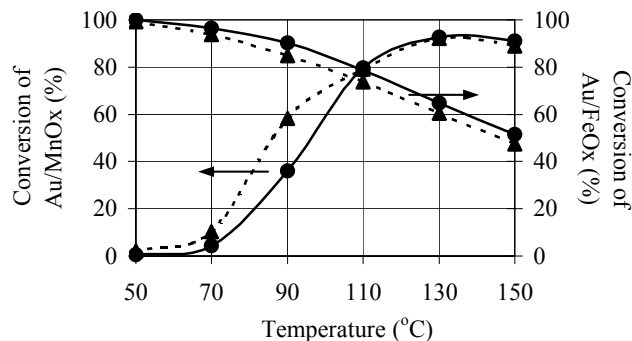


Figure 6. Effect of H₂O on the activity of both catalysts. Solid lines, 2.6% H₂O; dotted lines, 0% H₂O.

Conclusions

The activity of two kinds of catalyst has been studied for selective CO oxidation. It was found that Au/MnO_x gave 95% conversion and 60% selectivity at 130°C while Au/FeO_x gave >90% conversion and >50% selectivity at the temperature ranging from 50-90°C.

The composition of the reactant gas had a definite effect on the catalyst activity. Negative effect had been found for CO₂ and reverse for water.

Acknowledgement. This work was supported by the Petroleum and Petrochemical College, Chulalongkorn University, Bangkok, Thailand and partially supported by The Thailand Research Fund (TRF).

References

- (1) Sanchez, R. M. T.; Ueda, A.; Tanaka, K.; and Haruta, M. *J. Cat.*, **1997**, *168*, 125-127.
- (2) Kahlich, M. J.; Gasteiger, H. A.; Behm, R. J. *J. Cat.* **1999**, *182*, 430-440.
- (3) Hoflund, G. B.; Gardner, S. D. *Langmuir* **1995**, *11*, 3431-3434.
- (4) Haruta, M.; Tsubota, S.; Kobayashi, T.; Kageyama, H.; Genet, M.J.; Delmon, B. *J. Cat.* **1993**, *144*, 175-192.
- (5) Haruta, M. *Cat. Today* **1997**, *36*, 153-166.

IN-SITU IR STUDIES ON THE OXIDATIVE CARBONYLATION OF METHANOL TO DIMETHYL CARBONATE

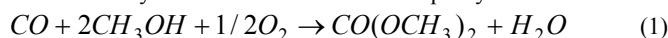
Xinbin Ma, Zhenhua Li, Baowei Wang, Genhui Xu

State Key Laboratory of C₁ Chemistry and Technology,
School of Chemical Engineering and Technology, Tianjin University,
Tianjin 30072, China

Introduction

Dimethyl carbonate (DMC) has been used as gasoline extender, an octane number improver and an organic solvent. Dimethyl carbonate is much less toxic than phosgene and dimethyl sulfate. Also, the by-product, when DMC was used to substitute for highly toxic compounds such as phosgene and dimethyl sulfate in many reactions, is methanol or carbon dioxide, which is easily separated from the product and leads to less pollution. So, the synthesis of DMC through an environmentally benign process attracts worldwide attention.

The traditional methods for DMC production are the phosgene-methanol and ester-exchange method¹. In these two methods, some raw materials are highly toxic and result in pollution, which limits its further application. The oxidative carbonylation of methanol to DMC as shown in reaction (1) is an environmentally benign process². It absorbed many researchers' attention in the past years.



Many researchers have studied this reaction but their work mainly focused on the catalytic activities of the catalysts, however, little has been reported on the mechanism of the reaction. In this work, the in-situ IR technique was used to study the reaction mechanism of oxidative carbonylation of methanol to dimethyl carbonate over supported Cu catalysts.

Experimental

The catalyst of Cu supported on Al₂O₃ with a Cu content 9 wt% was prepared by incipient wetness impregnated with an ethanol solution of CuCl₂. The impregnated sample was dried under a flow of nitrogen gas at 373 K for 3 h. The dried sample was cooled to room temperature and was further treated by incipient wetness impregnation with NaOH solution. Then the sample was subjected to a thermal treatment under a flow of nitrogen gas at 573 K for 3 h. The molar ratio of OH/Cu is 1, calculated from the moles of impregnated CuCl₂ and the moles of NaOH.

The activity of catalyst was measured with a micro catalytic reaction system comprising a stainless steel fixed bed reactor of 5 mm inner-diameter³, with a molar ratio of carbon monoxide to methanol of 1.3, a molar ratio of oxygen to methanol of 0.3. The conversion of methanol was 15.62%, and the selectivity to DMC was 62.43% at reaction temperature of 403 K and pressure of 0.7 MPa.

The IR spectra were obtained using a PE System FT-IR spectrometer. An in-situ infrared reactor cell, equipped with NaCl windows and capable of operating in the range 298 K to 773 K and 0.1 MPa to 2.0 MPa, was used for in-situ IR studies.

The powdered catalysts were pressed into a flake with diameter 12 mm and height 0.1 mm, placed in the reactor cell and purged the air from the reactor cell by nitrogen at flow rate of 5 SCCM. The temperature of the reactor cell was heated to 473 K at a rate of 5 K min⁻¹ in the nitrogen in order to clean the surface of the catalyst flake, after 10 minutes the reactor cell was controlled at 403 K and at a pressure of 0.7 MPa. IR data were collected at 4 cm⁻¹ resolution and 50 scans.

Results and Discussion

The oxygen, carbon monoxide and methanol was separately introduced the reactor cell in the reaction condition. Fig. 1 displays the in-situ IR spectra of adsorbed oxygen. The intensity of the band at 1292 cm⁻¹ increases with the increase of the adsorbed time, but the intensity of the band at 1186 cm⁻¹ doesn't change. When the oxygen is adsorbed on the supporter Al₂O₃ at the same condition, there is only band at 1186 cm⁻¹, the band at 1292 cm⁻¹ don't appear. So the band at 1292 cm⁻¹ and 1186 cm⁻¹ is attributed to the O₂ adsorbed on the catalyst and the supporter Al₂O₃, respectively. O₂ adsorbed on the catalyst is decomposed further.

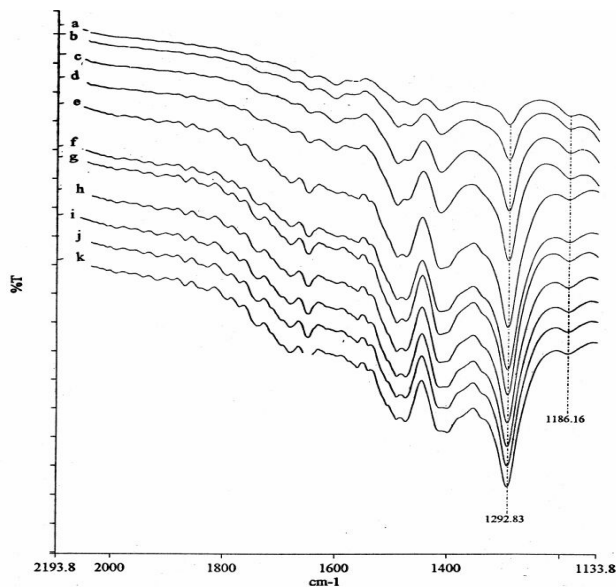


Figure 1. IR spectra for adsorption of O₂ on Cu/Al₂O₃ catalyst
a: 1'30", b: 3'30", c: 4'30", d: 7'50", e: 11', f: 13'30", g: 20',
h: 25', i: 30', j: 35', k: 40'

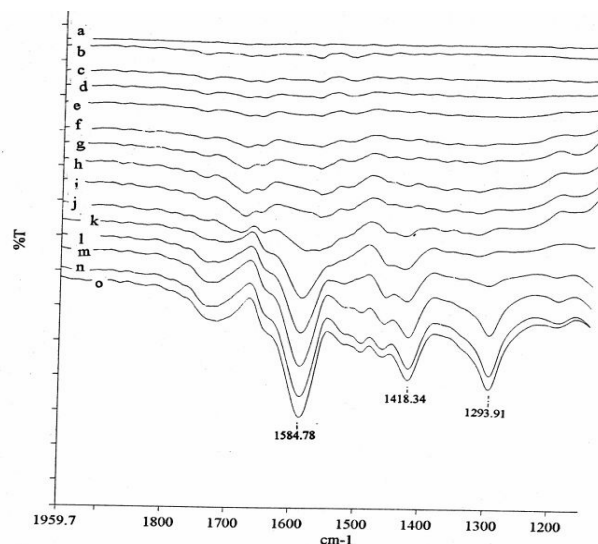


Figure 2. IR spectra for co-adsorption of O₂ and CO on catalyst
a: CO was introduced (0'), b: 2'40", c: 4'50", d: 6'50", e: 9'30",
f: 20', g: 30', h: 50', i: O₂ was introduced (51'), j: 54'15", k: 56',
l: 60', m: 64'30", n: 68'30", o: 75'35"

Carbon monoxide was introduced into the reactor cell, no any peaks were observed as shown in Fig. 2. This indicated that carbon monoxide was adsorbed weakly on the surface of the catalyst. When the oxygen and carbon monoxide were introduced the reactor cell together, not only the band at 1292 cm^{-1} , which is oxygen adsorbed on the catalyst, was observed, but also the band at 1585 cm^{-1} and 1418 cm^{-1} appear. This indicated that the oxygen and carbon monoxide are co-adsorbed on the catalyst.

IR spectra for adsorption of methanol on catalyst $\text{Cu}/\text{Al}_2\text{O}_3$ is shown in Fig. 3. The intensity of the band at 1111 cm^{-1} increased with the increase of the adsorbed time. The band at 1111 cm^{-1} is assigned to the methoxy group⁴, which indicated that methanol was adsorbed on the catalyst surface. When the pressure of the reactor cell was degraded to the 0.1 MPa and the nitrogen was introduced, the band of the methoxy group disappeared, only the band at 1056 cm^{-1} and 1032 cm^{-1} existed, which is attributed to the vapor methanol. The results indicated that the high pressure was favorable for the methanol adsorbed on the catalyst $\text{Cu}/\text{Al}_2\text{O}_3$ to produce methoxy group.

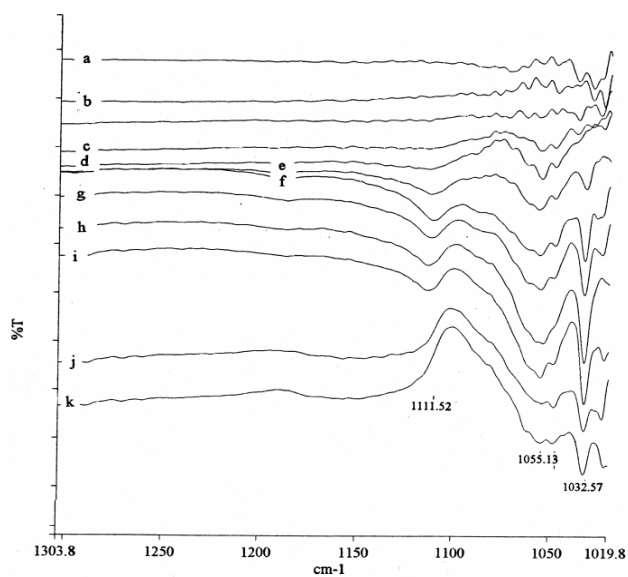
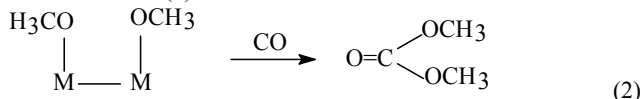


Figure 3. IR spectra for adsorption of methanol on catalyst a: methanol was introduced (0'), b: 2'5'', c: 6'37'', d: 12', e: 16'10'', f: 21', g: 30', h:40', i: 50', j: nitrogen was introduced (90'), k: 120'

IR spectra for in-situ oxidative carbonylation of methanol to DMC over $\text{Cu}/\text{Al}_2\text{O}_3$ catalyst are shown in Fig. 4. The oxygen, carbon monoxide and methanol were together introduced into the reactor cell, the band at 1171 cm^{-1} , which is assigned to the dimethyl carbonate, was observed⁵. According to the IR spectra of the in-situ reaction, the reaction mechanism may be the insertion reaction of weakly adsorbed carbon monoxide into the adsorbed methoxy groups as shown in reaction (2).



The molecular oxygen was adsorbed on the supported Cu catalyst and further decomposed. The methoxy groups might react with decomposed oxygen to produce carbon dioxide and water as shown in the reaction (3). So the concentration of oxygen should be controlled reasonably to avoid the oxidation of methanol to produce carbon dioxide.

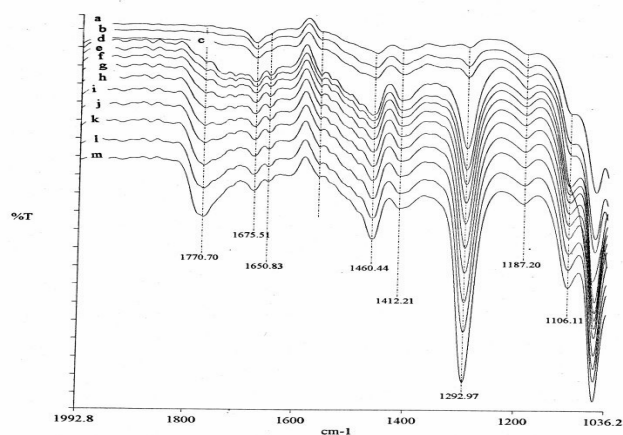
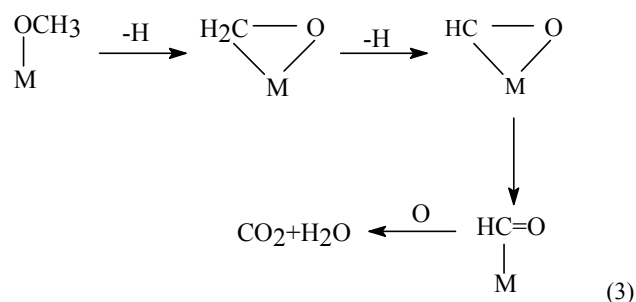


Figure 4. IR spectra for in-situ reaction on $\text{Cu}/\text{Al}_2\text{O}_3$ catalyst a: 2', b: 6'15'', c: 10'30'', d: 12'50'', e: 14'30'', f: 16', g: 18', h: 20', i: 25', j: 30', k: 35', l: 40', m: 45'

Conclusions

The in-situ IR technique was used to study the reaction mechanism of oxidative carbonylation of methanol to dimethyl carbonate over supported Cu catalysts. The results indicated that oxygen was adsorbed on the supported Cu catalyst and further decomposed. carbon monoxide was adsorbed weakly on the surface of the catalyst. The methoxy groups were found when methanol was introduced to the catalyst and higher pressure was favorable for the formation of methoxy groups. The reaction mechanism is the insertion reaction of weakly adsorbed carbon monoxide into the adsorbed methoxy groups. It was also found that methoxy groups might react with decomposed oxygen to produce carbon dioxide and water. So the concentration of oxygen should be controlled reasonably.

Acknowledgement. This work is supported by Natural Science Foundation of Tianjin in China. (973701711)

References

1. Gilpin, J. A. and Emmons, A. H. US Pat., 803201
2. David, S. G. and Staines, S. M. EP 134668
3. Ma, X. B.; Zhao, R. Z.; Xu, G. H.; He, F.; and Chen, H. F. *Catal Today*. **1996**, 30, 201.
4. Clarke, D. B. and Bell, A. T. *J. Catal.*. **1995**, 154(2), 314.
5. Schild, C.; Wokaun, A. and Baiker, A. *J. Mol. Catal.*. **1990**, 63(2), 223.

DIESEL FUEL FORMULATION EFFECTS ON INJECTION TIMING AND EMISSIONS

James Szybist, David Morris and André L. Boehman

The Energy Institute
The Pennsylvania State University
405 Academic Activities Building
University Park, PA 16802

Etop Esen

ConocoPhillips
600 N. Dairy Ashford
Houston, TX 77252

Introduction

Addition of biomass-derived fuels and synthetic fuels to diesel fuel basestocks is a means of producing a cleaner burning diesel fuel. Blending with oxygenated or zero sulfur fuels can lead to particulate emissions reductions by interfering with the soot formation process and by decreasing the formation of sulfates. However, in the case of biodiesel fueling (e.g., "B20", a blend of 20vol.% methyl soyate in diesel fuel) there is a well documented increase of 2-4% in NO_x emissions [1]. As shown by Van Gerpen and co-workers, the NO_x increase with biodiesel fueling is attributable to an inadvertent advance of fuel injection timing. The advance in injection timing is due to the higher bulk modulus of compressibility, or speed of sound, in the fuel blend, which leads to a more rapid transfer of the pressure wave from the fuel pump to the injector needle and an earlier needle lift [2,3].

In this paper, we examine this interaction between the bulk modulus of compressibility of various fuel samples and their effect on fuel injection timing. The fuels considered range from methyl soyate (the methyl ester of soybean oil), unrefined soybean oil, and paraffinic solvents to ultra low sulfur and conventional diesel fuels. Both the impact on injection timing and the variation in the bulk modulus of compressibility are measured so that correlation between fuel composition, fuel properties and injection timing can be observed and quantified.

Experimental

Two different experimental systems were used in the work described here: a high pressure viscometer, capable of measuring the bulk modulus of compressibility with the use of a pycnometer; and a highly instrumented, single-cylinder direct injection (DI) diesel engine, with an accompanying spray visualization chamber. The bulk modulus of various fuels was measured, and corresponding measurements were made of the impact of the fuel on the injection timing in the DI diesel engine.

High Pressure Viscometer. This instrument was developed for studies of the viscosity and bulk modulus of hydraulic fluids that contained dissolved gases [3]. The principle of operation for this device is that when a fluid is exposed to higher pressures, it will have a reduction in volume. The governing equation for the calculation of bulk modulus is:

$$B = (P - P_0) \cdot V_0 / (V_0 - V) \quad (1)$$

where B is the bulk modulus in psi, P is the measured pressure in psi, P₀ is atmospheric pressure, V₀ is the volume of the sample at atmospheric pressure and V is the volume at the new pressure.

The measurement equipment consists of a modified 21-R-30 Stainless Jerguson gage capable of handling pressures up to 4000 psi.

Two panels with viewing windows allow for viewing of the sample. Each window glass has two gaskets, one on either side, to ensure a tight seal on the chamber. For pressures in the range of 0-1000 psi, a direct connection to a helium gas cylinder provides the necessary pressure. For pressures above 2000 psi, a 4.5-liter Aminco hydrogenation bomb is filled with helium and oil is pumped into the bomb to achieve pressures up to 16000 psi. A constant temperature bath kept the pressure cell at a temperature of 100 degrees F. Bulk modulus is measured via a change in height within the pycnometer tube, as the pressure in the cell is varied. Water was used as a calibration standard.

DI Diesel Engine and Spray Chamber. A Yanmar L40 AE D air cooled 4-stroke DI diesel engine was coupled to an electric motor and motored at speed and fuel consumption conditions that simulated the G2 test modes from the ISO 8178-4.2 [4]. Only results from a load setting of 25% at 3600 RPM are presented here. The experimental system is shown schematically in Figure 1. The fuel consumption was measured by a gravimetric method using an Ohaus Explorer balance, accurate to 0.1g. The fuel injector was removed from the cylinder head and placed into a spray chamber with visual access to the fuel spray. The chamber was positioned so that the original high pressure fuel line could be used without modification of length, although it was necessary to bend the fuel line. Images of the spray were captured using an AVL 513 D Videoscope, an integrated triggering and digital imaging system. The triggering system operated with an AVL 364 shaft encoder mounted on the engine crank shaft, enabling 0.1 CA degree resolution.

The spray timing was also monitored with a light attenuation method. A Uniphase 0.95 mW Helium-Neon laser was positioned so that the laser beam intersected the fuel spray at the injector orifice. During the spray event the laser was attenuated, changing the output voltage and enabling a clear transition at both the beginning and end of the spray.

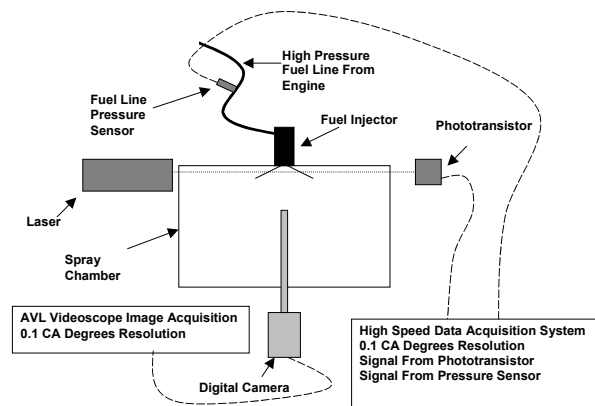


Figure 1. Schematic diagram of the spray visualization chamber connected to the DI diesel engine with access for digital imaging and laser attenuation measurements of fuel injection timing.

Fuel Samples. Fuel samples were selected to examine two separate issues with regard to fuel formulation and engine emissions. The first is verification of the observations of Van Gerpen and co-workers [2,3] regarding the difference in bulk modulus between biodiesel fuels and diesel fuel and the resulting effect on fuel injection timing. The second is examination of the potential impact of the use of paraffinic fuels, such as Fischer-Tropsch diesel fuels, on injection timing. To meet these objectives, the fuel samples tested were a biodiesel fuel (methyl soyate from World Energy), an unrefined soybean oil (from Agricultural Commodities, Inc., New Oxford, PA), Norpar-13 (a normal paraffin mixture from C₁₁ – C₁₅

from ExxonMobil), paraffinic distillate fuel, a 325 ppm conventional diesel fuel (from BP), and a 15 ppm sulfur diesel fuel (from BP).

Results and Discussion

Figures 2 and 3 show results from the measurements of injection timing and the bulk modulus of compressibility for diesel and biofuel blends. If one takes the indication of 0.4 relative spray intensity as an indication of the start of fuel injection, Figure 2 indicates that there is a 0.2 to 0.3 CA advance of fuel injection timing for the diesel-biodiesel (B20) and diesel – soy oil blends, while there is an advance of 1.0 CA with pure biodiesel (B100). Figures 3 and 4 show that the effect of the purely paraffinic fuels is to retard the fuel injection timing. The largest retardation is 0.5 CA., observed for Norpar, which also has the lowest bulk modulus. The paraffinic distillate yielded a 0.4 CA retardation of injection timing and has a bulk modulus that is lower than diesel fuel, but higher than Norpar.

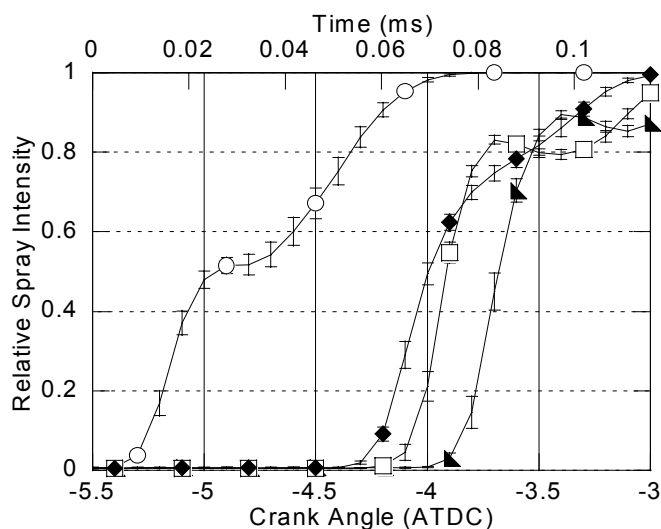


Figure 2. Measured fuel injection timing for biodiesel blends in conventional diesel fuel shown as relative spray intensity as a function of crank angle position relative to TDC. (▲) Baseline diesel fuel, (□) B20, (○) B100, (◆) 16vol.% Soy oil in diesel fuel.

Conclusions

The present work confirms previous observations on the impact of biodiesel fuels on fuel injection timing, that the higher bulk modulus of compressibility of vegetable oils and their methyl esters leads to advanced injection timing. This has been shown in the literature to contribute to the well-documented NO_x emissions increase with the use of biodiesel fuel. An opposite trend is observed with paraffinic fuels, which lead to a retarding of injection timing because they have a lower bulk modulus of compressibility than conventional diesel fuels and which supports the observation that paraffinic fuels such as Fischer-Tropsch diesel fuels yield lower NO_x emissions.

Acknowledgement. The authors wish to thank Dan Sharrer of Ag Com, Inc. for providing the soybean oil used in this study. This work was supported in part by the West Penn Power Sustainable Energy Fund.

This paper was written with support of the U.S. Department of Energy under Cooperative Agreement No. DE-FC26-01NT41098. The Government reserves for itself and others acting on its behalf a royalty-free, nonexclusive, irrevocable, worldwide license for Governmental purposes to publish, distribute, translate, duplicate, exhibit, and perform this copyrighted paper.

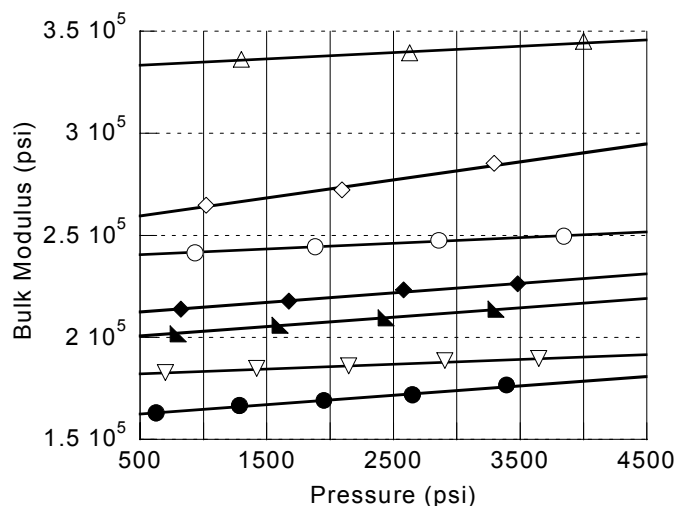


Figure 3. Measured bulk modulus of (Δ) Water, conventional and ultra low sulfur fuels, (◇) Soy oil, (○) Biodiesel, B100, (◆) 20% Soy oil blend in conventional diesel fuel, (▲) diesel fuel and (▽) paraffinic distillate and (●) Norpar-13 as a function of pressure.

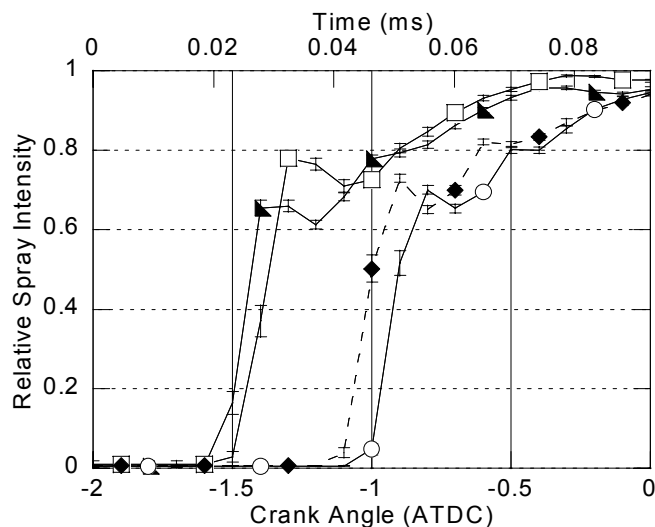


Figure 4. Measured fuel injection timing for paraffinic fuels versus conventional diesel fuel shown as relative spray intensity as a function of crank angle position relative to TDC. (▲) 15 ppm sulfur diesel fuel (BP15), (□) 325 ppm sulfur diesel fuel, (○) Norpar-13, (◆) paraffinic distillate.

References

- (1) Graboski, M.S. and R.L. McCormick, "Combustion of fat and vegetable oil derived fuels in diesel engines." *Progress in Energy and Combustion Science*, 1998, **24**(2): p. 125-164.
- (2) Monyem, A., J.H. Van Gerpen, and M. Canakci, "The effect of timing and oxidation on emissions from biodiesel- fueled engines". *Transactions of the ASAE*, 2001, **44**(1): p. 35-42.
- (3) Tat, M.E., et al., "The speed of sound and isentropic bulk modulus of biodiesel at 21 degrees C from atmospheric pressure to 35 MPa." *Journal of the American Oil Chemists Society*, 2000, **77**(3): p. 285-289.
- (4) O'Brien, J.A. "Precise Measurement of Liquid Bulk Modulus." M.S. Thesis, Penn State University, 1963.
- (5) ISO 8178: *Reciprocating internal combustion engines - Exhaust emissions measurement - Part 4. Test Cycles for different engine applications*. 1995, International Organization for Standardization.

ARTIFICIAL NEURAL NETWORK INVESTIGATION OF THE STRUCTURAL GROUP CONTRIBUTION METHOD FOR PREDICTING PURE COMPONENTS AUTO IGNITION TEMPERATURE

Tareq A. Albahri* and Reena S. George

Chemical Engineering Department, Kuwait University
P.O.Box 5969, Safat 13060, Kuwait

*Tel: (+965) 481-7662 (7459); Fax: (+965) 481-1772

E-mail: albahri@kuc01.kuniv.edu.kw

Web site: <http://www.albahri.info>

Introduction

In recent years, the term environmental impact has extended its traditional meaning to include other extensive concepts in view of the possibility of industrial accidents which, because of their magnitude, are capable of causing significant damage to people and the environment. This concern, which in the past was principally associated with the nuclear industry, now includes the chemical industry and their safety. Among these concerns are incidents of fire disasters caused by a leak of materials at or above their autoignition temperature in chemical and petrochemical plants.

Autoignition temperature is one of the most important safety specifications used to characterize the hazard potential of a chemical substance. As determined by ASTM standard test method E659-78¹, auto ignition temperature (AIT) is the lowest temperature at which the substance will produce hot-flame ignition in air at atmospheric pressure without the aid of an external energy source such as spark or flame. In the vernacular, autoignition temperature is the temperature at which a material will spontaneously burst into flames when exposed to the atmosphere. At the autoignition temperature, the rate of heat evolved by exothermic oxidation reaction overbalances the rate at which heat is lost to the surroundings and cause ignition. Autoignition temperature is dependent on the chemical and physical properties of the substance and the method and apparatus employed for its determination such as the volume and material of the vessel used, test pressure, and oxygen concentration¹. In the ASTM test method, autoignition temperature is determined by inserting a small test sample into a heated flask containing air at a predetermined temperature then observing in a dark room for a sudden appearance of a flame and a sharp rise in the temperature of the gas mixture. The test procedure is repeated for a series of prescribed sample volumes and the lowest predetermined internal flask temperature leading to said flame and temperature rise is taken to be the autoignition temperature. Autoignition temperature is also referred to as autogenous ignition temperature, spontaneous ignition temperature, or self-ignition temperature (SIT).

Since the quality of a fuel depends upon its composition, one could theoretically calculate the autoignition temperature from a comprehensive analysis of the individual components in a fuel and their contribution to the overall autoignition quality. Aside from the fact that a theory describing and quantifying the relationship between composition and autoignition has not yet been fully developed, the major obstacles to this approach is in the lack of a method to obtain the compositional data and in the scarcity of autoignition data for pure components. The former impediment is partially solved by the introduction of new analytical (gas and liquid chromatography) and theoretical techniques² while the latter which still awaits the introduction of new techniques for estimation, is solved in this work.

Technical Development

A careful examination of the autoignition temperature of hundreds of pure components reveals its complex dependency on the molecular structure. In this work we investigate this structural dependency of autoignition temperature using a structural group contribution approach which has been widely used in the past to predict many other physical and chemical properties³. For that purpose an artificial neural network was constructed using MATLAB code to test several structural group methods available in literature³ and assess their capacity to predict the autoignition temperature of pure components. The network structure is shown in Figure 1 and consists of three layers: input, output, and hidden. The input layer has a number of neurons which is equal to the number of structural groups being investigated. The hidden layer is a single layer with six neurons, and the output layer consists of one neuron.

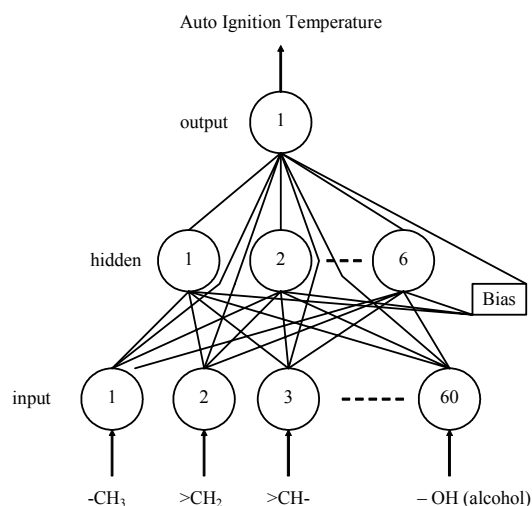


Figure 1. Architecture of artificial neural network for predicting the auto ignition temperature of pure components from their structural groups.

Results

Using the data on the autoignition temperature of 491 pure compounds from the AICHE-DIPPER⁴ database, several structural groups derived from the Joback group contribution approach³ were tested and modified for the location of the functional groups in the molecules. It was finally arrived at the set of groups that can best represent the experimental data with a correlation coefficient of 0.98 consisting of 60 structural groups shown in Table 1. A parity plot showing the accuracy of models predictions is presented in Figure 2. The average deviation in the predicted autoignition temperatures for all types of pure compounds ranging in AIT from 303 to 1283 K was 2.8%. The percentage errors for all 491 compounds are shown in Figure 3.

In conclusion, an estimation technique of the autoignition temperature of pure components, though essential, is inexistent. The group contribution approach presented here is the first and proves to be a powerful tool for predicting the autoignition temperature of pure components if coupled with a proper estimation technique such as neural networks. The clear advantage of the method is its ability to estimate accurately enough the AIT if the chemical structure only is known. This method is useful for the automatic generation and reliable estimation of AIT of pure components, for which no data

exists, with the objective of estimating AIT of petroleum fuels and others. At present the authors are diligently working on modifying the structural groups to improve the model predictions beyond the current results which further include determining the contribution values of these groups using optimization.

Table 1. Structural Groups Used to Estimate Pure Components Auto Ignition Temperature.

Serial no.	Group	Serial no.	Group
1	- CH ₃	31	- O - (ring)
2	> CH ₂	32	> C = O (ring)
3	> CH -	33	> NH (ring)
4	> C <	34	- N = (ring)
5	= CH ₂	35	- SiH
6	= CH -	36	> N - (ring)
7	= C <	37	- H
8	= C =	38	> Si <
9	≡ CH	39	- SiO
10	>CH ₂ (ring)	40	BH ₃
11	> CH - (ring)	41	- SiH ₂
12	> C < (ring)	42	- SO ₄
13	= CH - (ring)	43	> S
14	= C < (ring)	44	> SO
15	- F	45	- SH
16	- Cl	46	- SiH ₃
17	- Br	47	PH ₃
18	- OH (alcohol)	48	P
19	- O - (nonring)	49	P=S
20	O = CH - (aldehyde)	50	- CO-O-OC- (anhydride)
21	C = O (nonring)	51	Pb
22	- COOH (acid)	52	Na
23	- COO - (ester)	53	S
24	= O	54	- PO ₄
25	- NH ₂	55	= S
26	> NH (nonring)	56	≡ O
27	> N - (nonring)	57	- Cl (att. to CH ₃)
28	- CN	58	- Cl (att. to >CH ₂)
29	- NO ₂	59	- Cl (att. to >CH -)
30	- OH (phenol)	60	- Cl (att. to >C <)

Note: Groups 57 through 60 are for chlorine atoms in paraffinic compounds only.

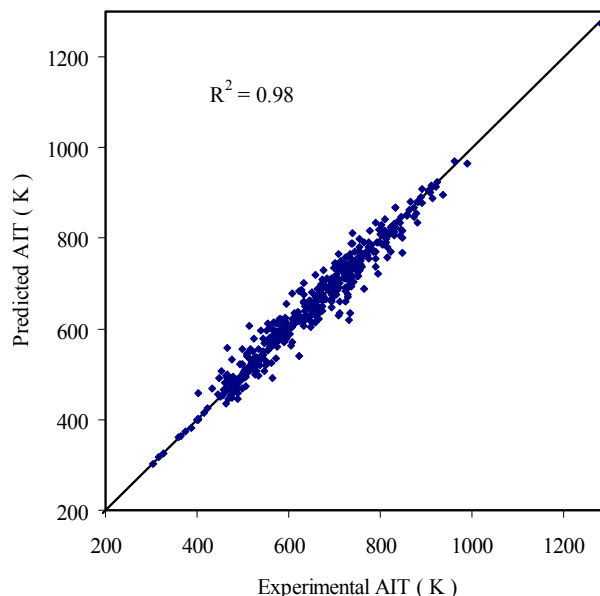


Figure 2. Parity plot for the Auto Ignition Temperature (AIT) of 491 pure components using the structural group contributions method and artificial neural networks.

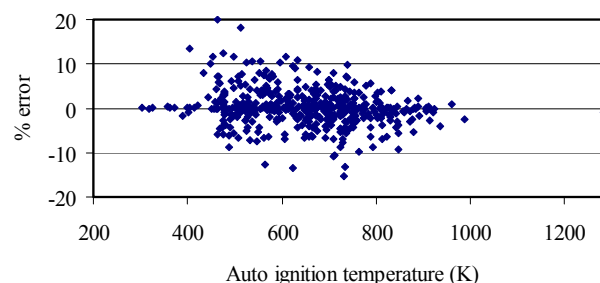


Figure 3. Percentage error range for the auto ignition temperature of 491 pure components using the structural group contributions method and artificial neural networks; 82% of data is below the 5% error range, 15% of data is between 5-10% error range, and only 3% of data is between 10-20% error range.

Acknowledgment

This work was supported by Kuwait University, Research Grant No. EC04/01.

References

- (1) ASTM International, *American Standards for Testing and Materials*, Designation: E659-78 (reapproved **2000**).
- (2) Neurock, M.; Nigam, A.; Trauth, D.; Klein, M.T, *Chemical Engineering Science*, **1994**, 49(24A), 4153-4177.
- (3) Reid, R.C.; Prausnitz, J.M.; Polling B.E.; *The properties of gases and liquids*, Hill: N.Y., **1987**.
- (4) American Institute of Chemical Engineers, *DIPPER Project 801Pure Component Data in DIPPRO*, public version, January 31, **1996**.

INVESTIGATION OF POLYCYCLIC AROMATIC HYDROCARBON COMPOUNDS (PAHs) ON FLUE GAS DESULFURIZATION (FGD) BY-PRODUCT

Ping Sun and Linda K. Weavers

Department of Civil and Environmental Engineering
and Geodetic Science, The Ohio State University
470 Hitchcock Hall
2070 Neil Avenue
Columbus, OH, 43210

Introduction

Flue Gas Desulfurization (FGD) technology has been widely used throughout the world in an effort to reduce acid rain from sulfur oxide (SO_x) emissions in coal combustion. Although this technology reduces SO_x emissions efficiently and cost effectively, the application of this technique leads to over 20 million metric tons of FGD by-product generated in the United States annually¹. Rather than dispose of FGD by-product as waste in landfills, efforts are underway to identify opportunities to reuse it^{2,3}. Prior to reuse, FGD by-product must be characterized for potential environmental hazards. Compared with inorganic components such as heavy metals on FGD by-product, organic components are expected to be present in lower amounts and consequently are often neglected. However, they may also have an important impact on the environment when FGD by-product is disposed or reused. Accordingly, research concerning concentration, fate (i.e., potential to leach into the environment), and minimization of organic components on FGD by-product is necessary.

Polycyclic aromatic hydrocarbons (PAHs) are regarded as recalcitrant compounds in the environment because PAHs show very slow release from solid phases such as soil and sediment. They are found worldwide, even in pristine areas such as the poles⁴. In addition, many PAHs are carcinogenic and/or mutagenic; therefore, they are of both environmental and health concern. A major source of PAHs in the environment is from fossil fuel combustion processes (i.e., coal burning)^{5,6}. Therefore, PAHs may exist on FGD by-product by deposition from flue gas or by mixing of fly ash carryover with FGD by-product.

The purpose of this study was to investigate the organic compounds, particularly PAHs, on FGD by-products. The correlations of PAHs on FGD by-products with other factors such as unburned carbon were also investigated.

Experimental

In this study, FGD by-product was sampled at boiler #8 at the McCracken Power Plant on The Ohio State University campus. A lime slurry mist is injected into the scrubber to react with sulfur oxides from flue gas leaving the boiler. The by-product, along with fly ash, is collected by filter bags in a pulse jet baghouse.

FGD By-product Sampling. Multiple grab samples were collected to fulfill a clean 950 mL brown glass bottle (cleaned by EPA procedures). Samples were subsequently stored in an environmental room (4 to 12°C) until the appropriate chemical measurement procedures were preformed.

Organic Chemical Analysis. For each sample, 10 g of FGD by-product was extracted in a Tecator Soxtec (Model 1043) extractor with CH₂Cl₂ for 5 hours. The solution from the extraction process was subsequently condensed to 1 mL prior to GC/MS analysis. EPA method 8270C provided the basis for measurement of polycyclic aromatic hydrocarbons (PAHs) and other semivolatile organic compounds. A Thermo-Finnigan GC/PolarisQ ion trap was used for

GC/MS analysis. Aliquots of 2 µL were injected into a Varian CP-5 fused silica capillary column (60m×0.25mm×0.25µm) by splitless injection mode. Helium served as the carrier gas. The mass spectrometer was operated in full scan mode for both standards and extracts. The PAHs and other semi-volatile compounds were identified by matching mass spectra to a NIST spectra database. Sixteen EPA-specified PAHs were confirmed using the retention times and quantified using calibration curves from the standard PAH compounds. The detection limits for these 16 PAHs are 0.1–1 ng/g, depending on the boiling point of the individual PAH.

Organic Carbon Content Measurement. Organic carbon content was measured by the STAR Laboratory of the Ohio Agricultural Research and Development Center (OARDC), OSU. Samples were “burned” under pure O₂ at 900°C on Elementar Americas, VarioMax Carbon/Nitrogen Analyzer to measure total carbon (TC). Total inorganic carbon (TIC) was determined by coulometry on an instrument manufactured by UIC Inc. Upon introduction of sample into the sample flask, the system was purged with a CO₂-free carrier gas to eliminate atmospheric carbon dioxide. Then, 2N HClO₄ was added, heated and inorganic carbon was oxidized to gaseous CO₂ that was measured by a CO₂-sensitive detector. The difference between TC and TIC is the organic carbon content.

Results and Discussion

In a preliminary study, a series of 10 FGD by-product samples doped with 100 ng surrogate (naphthalene-d₈) were extracted to measure the recovery rate of the extraction process. An average recovery rate of 85% was achieved. In addition, a mixture standard (16 different PAHs) containing 100 ng each PAH was added to four 10 g FGD by-product samples before extraction to measure the matrix recovery rate. **Fig 1** shows the average recovery rates ranged from 0–75% for the 16 different PAHs. The results indicate a low recovery rate and a decreasing recovery rate with an increase in molecular weight of the PAH. For PAHs larger than benzo(a)pyrene, they could not be extracted effectively.

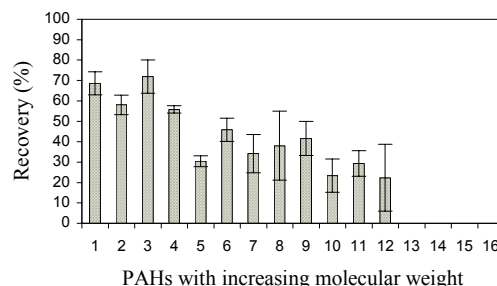


Figure 1. Recovery rate for 16 PAHs spiked onto FGD by-products.

Generally, several factors influence analyte recovery including matrix type, spike level, and total extraction time⁷. Compared with other studies and EPA standard methods on extraction of PAHs, the spike level in our experiments (10 ng/g) is much lower. For example, Chen *et al.* achieved recovery rates of deuterated PAHs ranging from 62% to 102% on coal tar contaminated soil with a matrix spike level of 20 µg/g⁸. However, since EPA standard method 3500B also recommends that the spike level should be 1 to 5 times higher than the concentration of the analyte in the real sample⁹, this unusually low matrix spike level was chosen to mimic concentrations expected for PAHs on FGD by-product. In addition, the FGD by-product is a complicated mixture of fly ash, lime, unburned carbon and other

materials. Because the organic matter content in the matrix plays an important role on adsorption of organic compounds¹⁰, the existence of unburned carbon in FGD by-product may also be one reason for the low recovery rate. The increasing of hydrophobicity of the PAHs with an increase in molecular weight may explain the decreasing recovery rate with increasing molecular weight. Currently, other extraction methods such as ultrasonic extraction are being developed to improve the recovery rate.

The identified PAHs on the collected FGD by-product samples were mainly 2-ring and 3-ring PAHs, such as naphthalene, acenaphthene, acenaphthylene, and phenanthrene; no large ring PAHs were found. The quantification data of detected PAHs (based on 4 experiments) on FGD-by product collected on different dates are shown in **Table 1**. The concentrations of these PAHs are low, usually less than a few ng/g. Other organic compounds were also found in the FGD by-product, for example, biphenyl and a series of n-alkanes. However, standards are needed to conclusively verify their existence.

Table 1. Concentration (ng/g) of Detected PAHs on FGD

Sample No.	Naphthalene	Acenaphthene	Acenaphthylene	Phenanthrene
1	2.53±0.24	N/D	N/D	0.37±0.27
2	1.51±0.06	N/D	N/D	N/D
3	2.94±0.20	N/D	0.58±0.02	0.36±0.25
4	5.92±0.22	N/D	N/D	0.67±0.46
5	2.12±0.12	0.98±0.03	0.83±0.03	0.33±0.19
6	2.44±0.14	0.66±0.02	0.46±0.02	0.40±0.27

N/D: not detected

Boiler operation parameters such as combustion temperature and excess air ratio during combustion have been shown to affect PAH formation¹¹. At the McCracken Power Plant, coal is burned at 1200°C and an air pump is used to provide excess air for combustion. The high combustion temperature will produce more energy to break the bonds of macromolecular PAHs in raw coal to form smaller size fragments. With the excess air, these fragments will further undergo oxidation reactions and produce more carbon dioxide and water in the flue gas. Therefore, the high combustion temperature and excess air may be the reason why small ring PAHs are the major compounds identified on FGD by-product¹². Another reason that large ring PAHs were not detected may be due to their low recovery rate. Since the large ring PAHs have higher affinities with the solid phase, they may strongly adsorb on FGD by-product and may not be easily extracted. Thus, the existence of large ring PAHs on FGD is still possible.

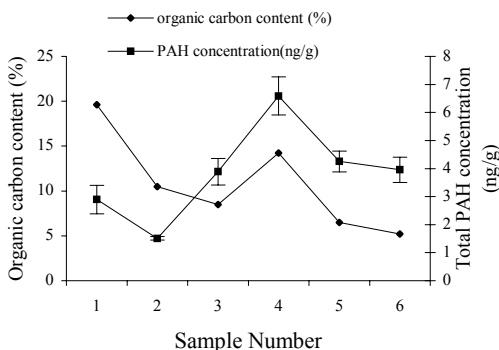


Figure 2. Measured total detected PAH concentration and organic carbon content of FGD by-products.

The organic carbon content on a weight percent basis and measured total PAH concentrations of 6 FGD by-product samples are shown in **Figure 2**. The results suggest a possible correlation between higher PAH concentrations and the organic carbon content in FGD by-product. Since unburned carbon is the major source of organic carbon in FGD by-product, unburned carbon is currently being separated from FGD by-product by initial sieving and following density separation using lithium heteropolytungstate (LST) solution. Measurement of PAH concentrations in separated unburned carbon parts will be performed to test the hypothesis.

Conclusions

This study has shown low recovery rates of PAHs in automatic Soxhlet extraction procedures. Several small ring (2 ~ 4-ring) PAH compounds were identified in FGD by-product, including naphthalene, acenaphthene, acenaphthylene, and phenanthrene. The concentrations of detected PAHs are usually less than a few ng/g. No large ring PAHs were detected, which may be attributed to low recovery rates. Initial indications suggest that concentrations of detected PAHs correlate with the organic carbon content in FGD by-product. Unburned carbon will be separated with initial sieving and density separation. PAH analysis of each size fraction will be carried out to verify the hypothesis that concentrations of detected PAHs correlate with the presence of unburned carbon in FGD by-product.

Acknowledgement The authors would like to thank the Ohio Coal Development Office (OCDO) and The Ohio State University for funding. Dr. Danold. W. Golightly's help with sampling and Mr. Kevin Jewell's help with organic carbon content measurement are gratefully acknowledged.

References

1. Stewart, B.R.; Kalyoncu, R.S.; *Proc. Int. Ash Utilization Symp.*, Lexington, KY, Oct., 1999.
2. Santhanam, C.J.; *Flue Gas Cleaning Wastes Disposal and Utilization*, Noyes Data Corporation: Park Ridge, New Jersey, 1981.
3. Lamminen, M.; Wood, J.; Walker, H. W.; Chin, Y-P.; He, Y.; Traina, S.; *J. Env. Quality*, **2001**, 30, 1371.
4. Henner, M.; Schiavon, M.; Morel, J.L.; Lichtfouse, E.; *Analisis*, **1997**, 25(9-10), M56.
5. Mastral, A.M.; Callen, M.S.; *Environ.Sci.Technol*, **2000**, 34(15), 3051.
6. Pisupati, S.V.; Wasco, R.S.; Scaroni, A.W.; *Journal of Hazardous Materials*, **2000**, 74(1), 91.
7. Dean, J.R.; *Extraction methods for environmental analysis*, John Wiley, Chichester: New York, 1998.
8. Chen, C.S.; Rao, P.S.; Lee, L.S.; *Chemosphere*, **1996**, 32(6), 1123.
9. U.S. Environmental Protection Agency, Method 3500B, Organic Extraction and Sample Preparation, 1996, U.S. Environmental Protection Agency
10. Watts, R.J.; *Hazardous Wastes: Sources, Pathways, Receptors*, John Wiley & Sons Inc: New York, 1997
11. Mastral, A.M.; Callen, M.S.; Mayoral, C.; Galban, J.; *Fuel*, **1995**, 74(12), 1762.
12. Liu, K.L.; Xie, W.; Zhao, Z.B.; Pan, W.P.; Rilly, J.T.; *Environ.Sci.Technol.*, **2000**, 34(15), 3177.

KINETICS OF CO₂-GASIFICATION OF SHENMU MACERAL CHARs

Qinglei Sun, Wen Li, Haokan Chen, Baoqing Li

(State Key Lab of Coal Conversion, Institute of Coal Chemistry,
Chinese Academy of Sciences, Taiyuan, 030001, China)

Abstract:

The gasification reactivity of Shenmu vitrinite and inertinite chars was investigated using TG-151 thermal balance. The gasification kinetics was analyzed using integral method, differential method and DAEM. The results showed that with increasing gasification temperature, the gasification reactivity of vitrinite and inertinite chars greatly increased. At the same gasification temperature, vitrinite char had higher gasification reactivity than inertinite char. The value of activation energy calculated using the three methods had the same order, inertinite char always had higher activation energy than vitrinite char, suggesting vitrinite char had higher gasification reactivity. The difference of the three methods was also compared. The integral and differential method can only supply the average of activation energy, while DAEM can supply the variation trends of activation energy during the whole gasification process. Therefore, DAEM was a better kinetics method comparing with the integral and differential method for description of the gasification process.

Keywords: maceral chars, CO₂ gasification, kinetics, integral and differential method, DAEM

ACTIVATION OF THERMAL PLASMA FOR COAL CONVERSION

Tian Yajun¹ Wang Baojun¹ Zhang Yueling² Zhang Yitgui³
Xie Kechang¹

1. State Key Lab of C1 Chemistry and Technology, Taiyuan
University of Technology, Taiyuan, 030024, P. R. China

2. Department of Applied Chemistry, Nanjing University of
Chemical Technology, Nanjing, 210009, P.R. China

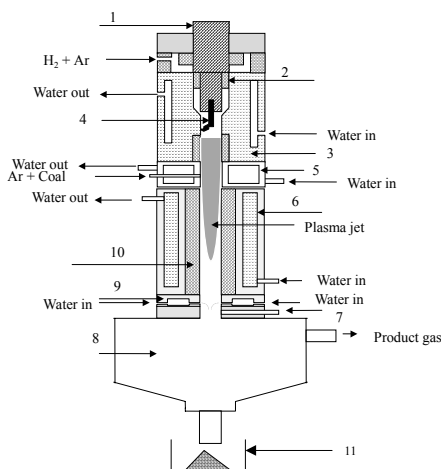
3. Jiaozuo Institute of Technology, Jiaozuo
454100, P.R. China

Introduction

Investigations¹⁻³ of coal conversion by arc plasma has been carried out for long time. Baumann et al.⁴ proposed that the release of volatile from coal was the first and an essential step as coal was injected into plasma jet. The generation of acetylene was contributed by the interaction of active species with the releasing volatile matter, after which the reactions stopped. Many publications reported that the active species such as energized ions and atoms had the capacity to convert coal directly even in low temperature^{5,6}. A plasma jet is a hot gas flow containing great deal of active species, so coal conversion in arc plasma jet is very complex. There still is not an agreement for the coal conversion under this condition.

Experimental

The experimental equipment is consisted of arc plasmatron, injector, reactor and quenching unit. The mixture of argon and hydrogen was the working gas of arc generator, their flow rate were 2.2 m³·h⁻¹ and 5.2 m³·h⁻¹. The effective power of plasmatron was 25.2 kW. The feedstock was injected into reactor through a tube with diameter of 5mm, the diameter of reactor tube is 20mm, and length is 350mm. Coal powder was carried into jet by argon with the flow rate of 1.7 m³·h⁻¹, and the coal feed rate ranged from 0.5~4.0g·s⁻¹ was controlled by the motor of feeder. The quenching unit was installed downstream position of reactor. A sampling position was sited between quenching unit and separator where the gas phase and the mixture of water and slag were separated. The gaseous products were vented from the outlet sited on the upper part of separator, and the condensed phase was discharged form the outlet sited at the bottom of separator to the filter unit where the slag were trapped. The structure scheme of equipment is shown in **Figure 1**.



1-Cathode 2-Insulation 3-Anode 4-Arc 5-Injector 6-Reactor
7-Sampling tube 8-Separator 9-Spray 10-Reactor wall 11-Filter
Figure 1 Diagram of experimental equipment.

The compositions of the product gases were measured by a special gas chromatography with two channels and three detectors (two FIDs and one TCD). Argon was used as tracer to calculate the amount of component in the product gas, and then coal conversion was determined. The chemical analysis data of Baode coal is shown in **Table 1**.

Table 1 Chemical analysis data of Baode coal

Proximate (wt%)			Ultimate (wt%)				
M _{ad}	A _d	V _{ad}	C _{daf}	H _{daf}	N _{daf}	S _{daf}	O _{daf}
4.43	3.29	40.35	75.82	5.36	1.86	0.74	16.22

Results

Effect of coal feed rate (CFR) on coal conversion

In our experiment, the coal feed rate (CFR) was controlled form 0.5 to 4.0 g/s. The power input and other conditions kept constant. **Figure 2** shows coal conversions as a function of CFR. It's found that as the increase of coal feed rate, the coal conversion increases. According to the Chinese Test Standard, the volatile content is 40.35% on the basis of air dry. The experiment results showed that the maximum coal conversion reached up to 55.58% on the same basis. The fact indicates that the maximum coal conversion could beyond coal volatile content, which implies not only pyrolysis but also some other factors have the contribution to the coal conversion.

Coal pyrolysis is an easy producer as coal was heated. It's believed that pyrolysis was the first conversion step under the condition of plasma jet with initial temperature of about 3700K. For the producer of devolatilization (pyrolysis), temperature is one of the key factors. As the increase of CFR, more energy was exhausted by the more reactions taking place under this condition, and more energy was consumed by the heat capacity of coal too. The average reaction temperature increased with the decrease of CFR. High temperature is in favor of conversion, so coal conversion increased as the decrease of CFR.

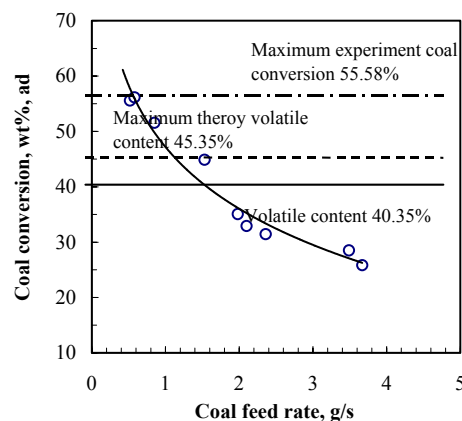


Figure 2 Coal conversion as a function of CFR

Effect of CFR on yield

Experimental results showed yields of CO and C₂H₂ decreased as the increase of CFR, as shown in **Figure 3**, while that of CH₄, C₂H₄+C₂H₆ increased somewhat. Volatile matter released from coal was the precursor of product gas such as C₂H₂ and CO. When CFR is decreased, coal specific energy (CSE) increased and coal conversion increased too, therefore, the yields of C₂H₂ and CO increased. As the increased of temperature the Gibbs free energy of C₂H₂ decreased and that of other hydrocarbons increased, that is C₂H₂ was more stable than other hydrocarbons. This is the reason that the yields of

other hydrocarbons such as CH_4 and $\text{C}_2\text{H}_4+\text{C}_2\text{H}_6$ decreased as the decrease of CFR shows in **Figure 3**.

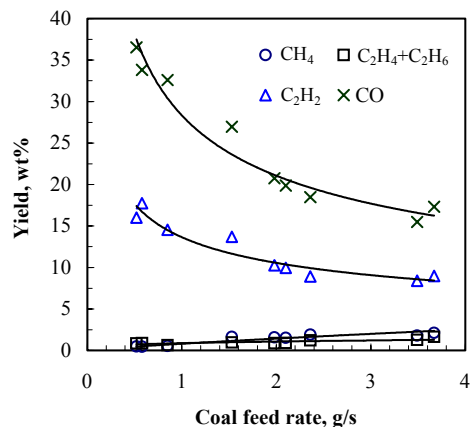


Figure 3 Effect of coal feed rate on the yield of the components in product gas

Effect of CFR on concentration

Although the yield of C_2H_2 decreased as the increase of CFR, it's found in **Figure 4** that its concentration increased as a function of CFR. Since great amount of hydrogen and argon were feed into as working gas of plasmatron, the maximum of C_2H_2 was only about 7% at larger CFR. As a desired product, high concentration means high output and hence the energy requirement for producing the acetylene decreased as the increase of CFR. Other components presented the similar regular as acetylene. Above all, raising CFR lead to the decrease of coal conversion, but increase of output of products.

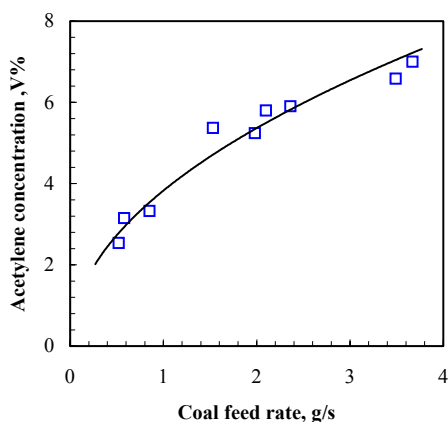


Figure 4 Acetylene concentration in product gas as a function of coal feed rate

Coal is the initial source of the product gas, a litter coal was fed a litter product was produced. So the concentration of product gas increased with CFR is reasonable, which has been discussed in literature⁷, although the yields of some products decreased as CFR. Since the improvement of concentration of one component, the output of it increased too. If the C_2H_2 was taken as a desired product, increasing the CFR is helpful for improving its produce cost.

Discussion

As far as pyrolysis is concerned the rapid pyrolysis can enhance coal conversion in some degree⁸. Azhakesan⁹ experiments indicated that rapid pyrolysis increased coal conversion about 5% of parent

coal in their experiment. Calculating according to their conclusion on the basis of air dry, the maximal theoretical conversion of Baode coal is about 45.35% that is far smaller than the maximum experiment result of 55.58% shown in **Figure 2**. As mentioned above, great deal of active species that can convert coal directly was contained in plasma jet, it is inferred active species played an important role for the coal conversion under this condition.

In experimental section a method of determining coal conversion was introduced, that is regarding the summary of the yields of components in product as total conversion (x_p). In so hot thermal jet, coal particles were heated rapidly; its maximum conversion should be 45.35% if only the pyrolysis producer happened. Assuming only the volatile matter were converted, taking the maximum theory volatile content (45.35%) as the volatile content of parent coal, then the conversion (x_v) can be determined by the expression

$$x_{V,ad} = V_{1,ad} - V_{2,ad} (1 - V_{1,ad} / 100)$$

Where, $V_{1,ad}$ is the maximum theoretical volatile content, and the $V_{2,ad}$ is the volatile content of the residual after reaction. **Table 2** is the conversion calculated according to the two methods. By comparing it's found they agree very well when the CFR is larger than $1.98 \text{ g}\cdot\text{s}^{-1}$. That means the CFR of $1.98 \text{ g}\cdot\text{s}^{-1}$ is a critical point. So it's inferred that when CFR was less than $2.0 \text{ g}\cdot\text{s}^{-1}$ both the pyrolysis and active species has the contribution to coal conversion, on the contrary, the coal conversion was governed mainly by the pyrolysis. This conclusion is first presented in this paper.

Table 2 Coal conversion calculated according to various methods

	Coal feed rate, $\text{g}\cdot\text{s}^{-1}$					
	0.52	0.58	0.85	1.98	3.49	3.67
$x_{V,ad}$	38.77	38.56	38.24	34.64	26.63	25.86
$x_{p,ad}$	55.58	56.13	51.55	35.08	28.52	25.83

Simulation based on CPD model was carried out.¹⁰ Three different coal feed rate of 0.58, 1.98 and $3.49 \text{ g}\cdot\text{s}^{-1}$, the comparison of calculation and experiment result is showed in **Figure 5**.

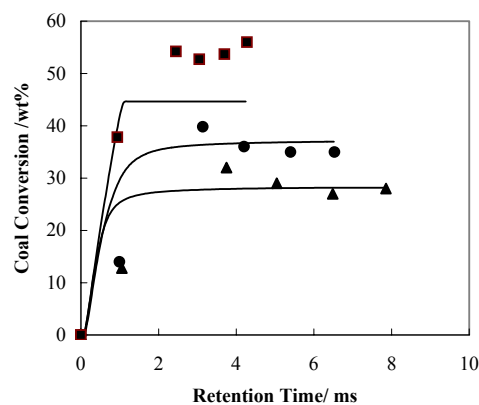


Figure 5 Coal conversion as a function of time at different coal feed rate. (■) $0.58 \text{ g}\cdot\text{s}^{-1}$ (●) $1.98 \text{ g}\cdot\text{s}^{-1}$ (▲) $3.49 \text{ g}\cdot\text{s}^{-1}$

For the case of $0.58 \text{ g}\cdot\text{s}^{-1}$, after the conversion predicted reached the value of 45%, it kept a constant without change. That is the maximal prediction did not match the maximal experiment value of 55.58%, but agreed with the maximal theoretical conversion. It also found that the CPD calculation has better agreement with the experiments with feed rates of 1.98 and $3.49 \text{ g}\cdot\text{s}^{-1}$, which was consistent with results shown in **Table 2**. In the CPD model, the

degree of conversion is mainly limited by the parameter of total bridge (p0) and char bridge (c0)¹¹. The labile bridges (p0-c0) were the main factor for conversion. The difference of the calculation from experiment implied that not only the labile bridges but also the char bridges and the bonds in cluster could be broken in this condition and hence the experiment had larger conversion than the CPD prediction. It was known that the interaction of active species could improve the coal conversion, but the thermal pyrolysis also played an important role in the coal conversion. In the case of low feed rate, both of them have large influence on the coal conversion. As the feed rate increases, the average impact of active species become weaker for its short life, and the conversion is mainly controlled by the thermolysis. It could be noticed that there was still larger difference in the first sampling position, which may be caused by the diffusion of heat and mass.

Conclusions

When coal was injected into plasma jet, the primary volatile was the product as coal was converted. It's found coal conversion decreased as the increase of CFR. Then the volatile matter was converted into gas products. The yields of CO and C₂H₂ decreased as the increase of CFR, and that of CH₄, C₂H₄+C₂H₆ increased somewhat. The concentration and output of components increased as the increase of CFR. Both coal conversion calculation and CPD simulation indicated that pyrolysis and the active species containing in plasma jet were the two main conversion routines. When CFR is less 2.0g·s⁻¹ both the pyrolysis and active species has the contribution to coal conversion, on the contrary, the coal conversion is governed mainly by the pyrolysis.

Acknowledgement

This work was financially supported by National Natural Science Foundation of China (No. 19935010); Natural Science Foundation of Henan Province of China.

References

- (1) Bond L R, Ladner W R and Mcconnel, G I T, *Fuel*, **1966**, 45, 381–395.
- (2) Chakravartty S C, Dutta D and Lahiri A, *Fuel*, **1976**, 55, 43–46.
- (3) Baumann H, Bittner D, Beiers H G, et al., *Fuel*, **1988**, 67, 1120–3.
- (4) Beier H G, Baumann H, Bittner D, et al, *Fuel*, **1988**, 67, 1012–1016.
- (5) Gill, P S, Toomy, R E, Moser, H C. *Carbon*, **1967**, 5: 43.
- (6) Sanada, Y, Berkowitz, N. *Fuel*, **1969**, 48: 375–379.
- (7) Xie K C, Tian Y J, et al., *J. Chem. Ind. & Eng.* **2001**, 52: 516–521.
- (8) Desypris, J, Murdoch, P, Williams, A. *Fuel*, 1982, 61: 807–816.
- (9) Azhakesan M., Bartle K. D. Murdoch P. L., et al., *Fuel*, **1991**, 70(3): 322.
- (10) Tian Y J, Xie K C, Zhu S Y, *Energy & Fuels*, **2001**, 15(6): 1354 – 1358.
- (11) Fletcher, T. H.; Kerstein, A. R. *Energy & Fuels*. **1992**, 6, 414–431.

A NEW PHYSICAL CONSTANT AND ITS APPLICATION TO CHEMICAL ENERGY PRODUCTION

By Andrew Anthony Angus, andrewangus@yahoo.com

1435 Olympic Drive, Milpitas, CA 95035

Keywords: Angus' constant, Angus photon, photochemical effect

Introduction

What is a physical constant? The author's own definition of physical constant is as follows: A **physical constant** is a numerical value that reveals a constant relationship between or among measurable characteristics of an object or event.

The Planck's constant is one important physical constant in physics. The pi is a numerical constant so essential in mathematics.

What is the significance of a physical constant?

Physical constants are constant numerical values that are important to physical sciences for many reasons:

- Physical constants simplify the understanding of a puzzling phenomenon.
- Physical constants integrate or relate different measurable characteristics of an object or phenomenon observed, which at first, may seem unrelated at all.
- Physical constants can be used in solving simple or complex equations that describe a simple or complex physical phenomenon.
- Physical constants can be used to discover new or more complex phenomenon which can never be discovered if the physical constant is not discovered in the first place.

In this paper, the author reveals a new physical constant which he simply calls the "Angus' constant". This new physical constant is equal to 1.98×10^{-25} J-m. The author uses the Greek letter lambda in upper case (Λ) to represent this new physical constant.

Finally, in this paper, the author reveals the application of this new physical constant to chemical energy production.

Review Of Related Literature

Max Planck discovered a constant numerical relationship between energy and frequency. This constant numerical relationship between energy and frequency is now called the Planck's constant (h).

$$h = 6.626 \times 10^{-34} \text{ J-s} \quad (\text{eq. 1})$$

Furthermore, Max Planck proposed in 1900 that energy can be absorbed or emitted in packet form or in "quantum" form by matter to explain the emission spectrum of thermal radiation. (Krane p.65) For many years, the scientific community did not accept Planck's radical idea that light can be absorbed or emitted by matter in packet form called "quantum" of energy. Planck suggested that energy is in the form of "quantum" and represented by the equation 2 (Halliday and Resnick p.1097):

$$E = nh\nu \quad n = 1, 2, 3, \dots \quad (\text{eq.2})$$

Legend: E is energy, n is the quantum number, h is the Planck constant, ν is the oscillation frequency.

Meanwhile, in 1905 Albert Einstein suggested that light energy behave as localized bundles later called "photon". (Krane p.67 and Halliday and Resnick p. 1103) The photon's energy has the equation:

$$E = h\nu \quad (\text{eq. 3})$$

Planck's quantum of energy equation (eq.2) and Einstein's photon energy equation (eq. 3) are related.

For many years, Albert Einstein and Robert Millikan helped Planck's radical idea of a quantum of energy to be accepted in the skeptical scientific community.

Einstein applied Planck's radical idea to explain a strange physical phenomenon whereby the electrons are emitted from a surface metal. Einstein called the phenomenon "photoelectric effect". In equation form:

$$\text{Net K.E. (electron)} = h\nu - W \quad (\text{eq.4})$$

Legend: h is the Planck constant, ν is the frequency, W is the work function.

When Einstein's equation was proven to be valid by the experiment of Robert Millikan, Planck's radical idea that radiation can be absorbed or emitted by matter in packet or "quantum" form became acceptable to the physics community.

Max Planck was awarded the Nobel Prize in Physics in 1918 for his discovery of Planck's constant (h) and the quantum nature of radiation. Albert Einstein was awarded the Nobel Prize in Physics in 1921 for applying Planck's quantum of energy to explain the photoelectric effect. Robert Millikan was awarded the Nobel Prize in 1923 for verifying by experiment Einstein's Law of photoelectric effect. (www.nobel.se)

Discussion

A. Derivation of the Angus' constant

The author derived the Angus' constant by studying the data gathered by previous scientists. The author observed the following values in the Lyman series which he made into a three-column table as in Table 1.

The values of photon energy (1st column) and photon wavelength (2nd column) were taken from a physics textbook *Modern Physics* by Kenneth Krane in p. 167. The third column was made by the author by multiplying the 1st column and 2nd column.

Table 1: The Lyman Series

Photon Energy (ev)	Photon Wavelength (nm)	Product (ev-nm)
10.20	121.5	1239.300
12.09	102.5	1239.225
12.76	97.2	1240.272
13.06	94.9	1239.394
13.23	93.7	1239.651
13.60	91.1	1238.960

How did the author derive the Angus' constant? There are two methods to derive the Angus' constant.

1. First Method

Step 1. The author multiplied the values of the photon energy with the photon wavelength of the Lyman series and obtained a product placed in the third column.

Step 2. The author observed that the photon emissions in the Lyman series have a constant product of around 1239 eV-nm as can be seen in the third column. The average value of the third column is 1239.467 eV-nm which I round off to 1239 eV-nm.

Step 3. The author converted the product of 1239 eV-nm into S.I. units (i.e. International System of Units or System Internationale units) using J-m.

Given the following conversions:

$$1 \text{ m} = 1 \times 10^9 \text{ nm} \quad (\text{eq. 5})$$

$$1 \text{ nm} = 1 \times 10^{-9} \text{ m} \quad (\text{eq. 6})$$

$$1 \text{ eV} = 1.602 \times 10^{-19} \text{ J} \quad (\text{eq. 7})$$

Legend: m is meter, nm is nanometer, eV is electron volt, J is Joules.

Let us convert the constant 1239 eV-nm in terms of S.I. units in J-m as follows:

$$1239 \text{ eV-nm} \times (1 \times 10^{-9} \text{ m/nm}) \times (1.602 \times 10^{-19} \text{ J/eV}) = 1.98488 \times 10^{-25} \text{ J-m} \quad (\text{eq. 8})$$

Step 4. We derive a new physical constant after assigning the constant value with the Greek letter lambda in upper case Λ and label it as the Angus constant.

$$\text{Angus' constant} = \Lambda = 1.98488 \times 10^{-25} \text{ J-m} \quad (\text{eq. 9}).$$

2. Second Method

An alternative method of deriving the Angus' constant is as follows:

Step 1. The author observed that energy (E) is inversely proportional to wavelength (w) as seen in Table 1. As energy (E) of photon increases, the wavelength (w) of the photon decreases. As energy (E) of photon decreases, the wavelength (w) of the photon increases. In equation form:

$$E \rightarrow 1/w \quad (\text{eq. 10})$$

Step 2. We multiply both sides by w and we get:

$$E \times w = 1 \text{ or unit constant} \quad (\text{eq. 11})$$

Step 3. Let us assign this unit constant as the Greek letter lambda in upper case.

$$E \times w = \Lambda \quad (\text{eq. 12})$$

Step 4. By filling the values for E and w, we can get the product value of Λ in terms of eV-nm in the third column of Table 1.

$$E = 10.2 \text{ eV}, w = 121.5 \text{ nm}, \quad (\text{eq. 13})$$

$$E \times w = 10.2 \text{ eV} \times 121.5 \text{ nm} \quad (\text{eq. 14})$$

$$E \times w = 1239.3 \text{ nm} \quad (\text{eq. 15})$$

$$\text{Round off} = 1239 \text{ nm} \quad (\text{eq. 16})$$

Step 5. Let us convert this product value 1239 eV-nm unit to S.I. units, that is, J-m unit as in equation 8.

$$1239 \text{ eV-nm} \times (1 \times 10^{-9} \text{ m/nm}) \times (1.602 \times 10^{-19} \text{ J/eV}) = 1.98488 \times 10^{-25} \text{ J-m} \quad (\text{as in eq. 8})$$

Step 6. Let us assign this product value as the unit constant or the Greek letter lambda and label it as the Angus' constant.

$$\text{Angus' constant} = \Lambda = 1.98 \times 10^{-25} \text{ J-m} \quad (\text{as in eq. 9})$$

So far, I have revealed two (2) ways on how to derive the new physical constant which I simply call the Angus' constant.

Let us now define the Angus' constant. The **Angus' constant** is a constant numerical value that relates the inverse relationship of energy and the wavelength of the photon.

B. Significance of the Angus' constant

What is the significance of the Angus' constant to the physical sciences?

1. The Angus' photon

Max Planck discovered the 'frequency' characteristic of the energy in quantum form in 1900. On the other hand, Albert Einstein proposed light can be emitted in particle form called "photon" in 1905. Both Planck and Einstein used the frequency (ν) in their equation as follows:

$$\text{Planck's quantum of energy: } E = nh\nu \quad (\text{similar to eq. 2})$$

$$\text{Einstein's photon energy: } E = h\nu \quad (\text{similar to eq. 3})$$

Equation 2 is what I call "Planck's quantum energy equation". Equation 3 is what I call "Einstein's photon energy equation".

On the other hand, the author discovered the 'wavelength' characteristic of the photon's energy. Let the Greek letter in upper case Λ be the Angus' constant and the letter w be the wavelength. The slash symbol (/) is a division operation sign.

$$\text{Angus' photon energy: } E = \Lambda/w \quad (\text{eq. 17})$$

Equation 17 is called "Angus' photon energy equation". Equation 17 was derived from Equation 12.

The **Einstein photon** is the photon represented mathematically in terms of frequency and the Planck constant. The Einstein photon: $h\nu$

The **Angus photon** is the photon represented mathematically in terms of wavelength and the Angus constant. The Angus photon: Λ/w .

The "Einstein photon" and the "Angus photon" are two ways of representing the Planck's "quantum" of energy radiation and absorption.

The author would like to emphasize that there is only one kind of quantum of light called photon which can be represented mathematically in two ways: a. in terms of its frequency characteristic as revealed by Albert Einstein, b. in terms of its wavelength characteristic as revealed by the author.

2. Dual Nature of Light

The debate on the nature of light has raged the physics community for hundreds of years starting in the 17th century between Isaac Newton and Christian Huygens.

Some physicists like the Dutch physicist-astronomer, Christian Huygens (1629-1695) believed that light has only one nature: wave nature. I call these group of physicists supporting the wave theory of light as “wave theorists”. Huygens was the chief advocate of the wave theory of light.

Some physicists like the English physicist, Isaac Newton (1642-1727) believed that light has only one nature: particle nature. I call these group of physicists supporting the particle nature of light as “particle theorists”. Newton was the chief advocate of the particle nature of light.

The “particle theorists” gained the upper hand when Max Planck discovered the discrete or “quantum” nature of radiation in 1900. Furthermore, Albert Einstein proposed that light energy travels in particles called “photons” in 1905.

If the Dutch physicist-astronomer Christian Huygens were alive today, he will surely be happy to find out that his wave theory of light is still valid because the author discovered the wavelength characteristic of the photon.

3. Dual Nature of Photon

The photon is supposed to be a discrete “particle” of light.

Question: Does the photon have wave characteristics? Answer: Yes. The author believes the photon has wave characteristics. The equation of the Angus’ photon (Λ / w) reveals the wave characteristic of the photon.

The “Angus constant” is significant to physical sciences because the new physical constant leads to the concept of the “Angus’ photon”, which in turn, helps to affirm the dual nature of the photon i.e. photon has two major characteristics: wavelength (w) and frequency (f).

The dual nature of the photon is affirmed because Einstein revealed in equation form the frequency characteristic of the photon while the author revealed in equation form the wavelength characteristic of the photon.

The photon although it is a particle can behave like a wave by virtue of its wavelength characteristic. Hence, the photon has a dual nature. A photon is a particle with a wave characteristic at the same time.

C. Applications of the Angus’ constant

The applications of the Angus constant are as follows:

1. Law of Photoelectric Effect

We can also use the Angus’ constant to give an alternative explanation to Einstein’s Law of Photoelectric Effect. The mathematical equation of the emission of electron from a metal surface is known as the “Einstein’s Law of Photoelectric Effect”.

$$\text{Net KE of electron} = h\nu - W \quad (\text{same as eq.4})$$

We can transform the well-known “Einstein equation” (eq. 4) into an “Angus equation” by substituting Einstein’s photonic energy ($h\nu$) with Angus’ photonic energy (Λ / w). The resulting equation is as follows:

$$\text{Net KE of electron} = \Lambda / w - W \quad (\text{eq. 18})$$

What is the meaning of the equation 18?

Equation 18 shows that the energy of the photon (Λ / w) is absorbed by the electron. Then, an energy is needed to overcome the work function (W) which prevents the electron from escaping the atom. The difference between the energy (Λ / w) and the work function (W) is the net kinetic energy (KE) of the electron. A critical wavelength (w) is necessary to induce the emission of electron from the surface of the metal.

A series of electron emissions from the metal surface would be a source of useful energy because these electron emissions possess a net kinetic energy in the form of photonic energy (Λ / w).

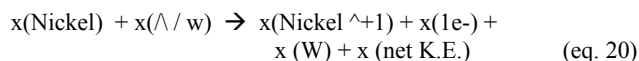
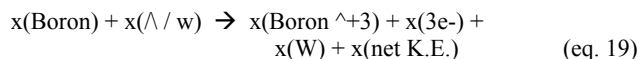
This is one application of the Angus’ constant (Λ) to energy production as revealed in equation 18.

Equation 18 is what the author simply calls the “Angus’s Law of Photoelectric Effect”. The **Angus’ Law of Photoelectric Effect** can be stated formally as follows:

An element or metal that is exposed to radiation will emit electrons: (a.) if the radiation that is absorbed in the form of an Angus’ photon (Λ / w) has the critical wavelength (w) and (b.) if the electron overcomes the potential energy (W) of its orbital. Otherwise, the electron will remain bound to the atom.

2. Chemical Reaction Equations

We can demonstrate the “photoelectric effect” phenomenon in chemical reaction equations as follows:



The chemical reaction equations 19 and 20 show that a useful energy can be produced due to the emissions of electrons which carry the net kinetic energy (net K.E.). The letter W is the amount of energy to overcome the energy barrier or work potential that prevents the escape of electron. The letter x is a coefficient that stands for the number of atoms absorbing the Angus’ photon (Λ / w).

The total useful energy that can be produced depends on the number of atoms (x) absorbing the Angus photon (Λ/w) and the critical wavelength (w) of the radiation.

3. Chemical Bond Breaking

The Angus photon is also useful in explaining the net energy that results when chemical bonds are broken.

The chemical bonds of 1 mole of chlorine gas needs a input energy of 242 KJ/ mol to break up. (Masterton p.280)

A chemical bond can be broken if the energy absorbed by the chlorine molecule is greater than the bond energy (K) that keeps the chemical bond intact. Let the energy barrier of a chemical bond be K. In the case of chlorine gas, bond energy $K = 242 \text{ KJ / mol}$. The initial photon energy absorbed by the chemical bond is Λ/w . If the initial photon energy that is absorbed by the chemical bond is greater than the “chemical bond energy barrier” K, the chemical bond will break. In equation form:

$$\text{Net KE} = (\Lambda/w) - K \quad (\text{eq. 21})$$

Eq. 21 is called the “Angus’ Law of Photochemical Effect”. The **Law of Photochemical Effect** can be formally stated as follows: A chemical bond of a molecule will break if the chemical bond absorbs a photonic energy (Λ/w) which is greater than the chemical bond energy barrier (K) that holds the chemical bond intact.

4. Chemical Energy Production

Sample Problem: How much net kinetic energy (net KE) can be produced when 1 mole of chlorine gas absorbs a radiation with a wavelength of 335 nanometers ? The solution is as follows.

The chemical bond of a chlorine gas Cl_2 can be broken if it absorbs energy of 242 KJ/mol. (Masterton p. 280)

Radiation of wavelength 335 nm corresponds to how much energy E ?

$$E = \Lambda/w \quad (\text{Angus photon energy equation}) \quad (\text{same as eq.17})$$

$$w = 335 \text{ nm} \times (1 \text{ m} / 1 \times 10^9 \text{ nm}) = 3.35 \times 10^{-7} \text{ m} \quad (\text{eq. 22})$$

$$E = (1.98 \times 10^{-25} \text{ J-m}) / 3.35 \times 10^{-7} \text{ m} \quad (\text{eq. 23})$$

$$E = 5.9 \times 10^{-19} \text{ J}$$

$$(\text{This is absorbed by 1 molecule of chlorine gas.}) \quad (\text{eq. 24})$$

$$\text{Energy per molecule} = E/\text{molecule} = 5.9 \times 10^{-19} \text{ J/ molecule of chlorine gas} \quad (\text{eq. 25})$$

This amount of “energy per molecule” of chlorine gas is equivalent to how much “energy per one mole” of chlorine gas molecule?

$$6.022 \times 10^{23} \text{ molecules} = 1 \text{ mole} \quad (\text{Avogadro's Number}) \quad (\text{eq. 26})$$

$$\text{Energy per mole} = E/\text{mol} = \text{J/molecule} \times \text{Avogadro's Number} \quad (\text{eq. 27})$$

$$E/\text{mol} = (5.9 \times 10^{-19} \text{ Joules / molecule}) \times (6.022 \times 10^{23} \text{ molecules/ mole}) \quad (\text{eq. 28})$$

$$E/\text{mol} = 355,927.16 \text{ Joules/ mole} \quad (\text{eq. 29})$$

$$\text{In terms of KJ/mol: } 355,927.16 \text{ Joules/mole} \times 1\text{KJ} / 1000 \text{ J} = 355.9 \text{ or } 356 \text{ KJ/ mol} \quad (\text{eq. 30})$$

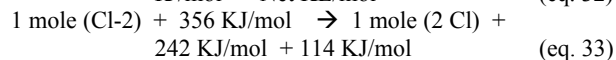
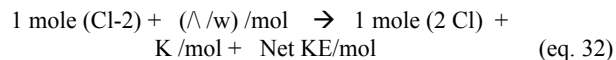
Let us now answer the question of the sample problem: How much is the net kinetic energy produced when 1 mole of chlorine gas absorbs a radiation with a wavelength of 335 nanometers ?

$$\text{Net K.E.} = \Lambda/w - K \quad (\text{Angus Law of Photochemical Effect}) \quad (\text{same as eq.21})$$

$$\text{Net K.E.} = 356 \text{ KJ} - 242 \text{ KJ} = 114 \text{ KJ} \quad (\text{eq. 31})$$

The net kinetic energy produced is 114 Kilojoules. This is the net amount of useful chemical energy that is carried by 1 mole of chlorine gas.

The breaking of chemical bonds involving energy absorption in the form of chemical reaction equation is as follows:



The total photonic energy per mole or $[(\Lambda/w)/\text{mol}]$ that is absorbed by 1 mole of chlorine gas molecule is 356 KJ/ mol. The total energy per mole needed to break the chemical bond energy barrier (K) of 1 mole of chlorine gas molecule is 242 KJ/ mol. The total net energy per mole carried by one mole of chlorine gas is 114 KJ/mol.

Equation 33 is balanced in terms of mass and energy (i.e the reactant side is equal to the by-product side):

$$\text{In terms of mass: } 1 \text{ mole of } \text{Cl}_2 = 1 \text{ mole of } 2 \text{ Cl} \quad (\text{eq.34})$$

$$\text{In terms of energy: } 356 \text{ KJ/ mol} = 242 \text{ KJ/ mol} + 114 \text{ KJ/mol} \quad (\text{eq.35})$$

As we can see in the sample problem, the “Angus’ Law of Photochemical Effect” is also useful in computing the total energy or the total net kinetic energy that results in the breaking of chemical bonds.

Conclusion

The prevailing notion about photon is that photon has a frequency characteristic but not having a wavelength characteristic. The author reveals in equation form that photon has a wave characteristic in the form of Λ/w .

This paper gives an alternative or new interpretation of the photoelectric effect phenomenon using the Angus’ constant. This new interpretation is embodied in equation form called the Angus’ Law of Photoelectric Effect.

The “Angus’ Law of Photoelectric Effect” and the “Angus’ Law of Photochemical Effect” are simply two of the many applications of the Angus’ constant to energy production.

Other applications of the Angus’ constant or Angus’ photon to energy production will be discussed in future papers.

Summary

1. There are two important physical constants related to the photon, namely: the Planck’s constant (h) and the Angus’ constant (Λ)

2. The photon can be mathematically represented in two ways: Einstein’s photon (hf) and Angus’ photon (Λ/w).

3. The Angus photon is useful in explaining the escape of electrons from atoms with the aid of light (i.e. photoelectric effect) and breaking of chemical bonds with the aid of light (i.e. photochemical effect).

4. The “Angus’ Law of Photoelectric Effect” is useful in calculating the net kinetic energy of escaping electrons from atoms.

5. The “Angus’ Law of Photochemical Effect” is useful in calculating the net kinetic energy that results after the breaking of chemical bonds.

Equation Summary

- | | | |
|--------------------------------------------|----------------------------------------------|--------|
| 1. Planck’s Constant: | $h = 6.626 \times 10^{-34} \text{ J-s}$ | eq. 1 |
| 2. Angus’ Constant: | $\Lambda = 1.98 \times 10^{-25} \text{ J-m}$ | eq. 9 |
| 3. Planck’s Quantum Energy Equation: | $E = nh\nu \quad n = 1, 2, 3, \dots$ | eq. 2 |
| 4. Einstein’s Photon Energy Equation: | $E = h\nu$ | eq. 3 |
| 5. Angus’ Photon Energy Equation: | $E = \Lambda / w$ | eq. 17 |
| 6. Einstein’s Law of Photoelectric Effect: | $E = h\nu - W$ | eq. 4 |
| 7. Angus’ Law of Photoelectric Effect: | $E = \Lambda / w - W$ | eq. 18 |
| 8. Angus’ Law of Photochemical Effect: | $E = \Lambda / w - K$ | eq. 21 |

Reference

1. Masterton, William, Emil J. Slowinski, and Conrad L. Stanitski. (1981) “Chapter 9: Chemical Bonding” In: *Chemical Principles*. 6th ed. New York and Philadelphia: Saunders College Publishing. pp.258-283
2. Krane, Kenneth. (1983). *Modern Physics*. New York: John Wiley and Sons.
3. Halliday, David and Resnick, Robert.(1986) *Physics Part 2 Extended Version*. 3rd ed. New York: John Wiley and Sons.
4. Kogan, V. I. (2000) “The discovery of the Planck constant” In: *Uspekhi* 43 (12) 1253-1259 (2000).
5. “The Nobel Prize in Physics -- Laureates: 1918 Max Planck”. In: *Nobel E-Museum*. www.nobel.se.
6. “The Nobel Prize in Physics -- Laureates: 1921 Albert Einstein”. In: *Nobel E-Museum*. www.nobel.se.
7. “The Nobel Prize in Physics -- Laureates: 1923 Robert A. Millikan”. In: *Nobel E-Museum*. www.nobel.se.

CO-PRODUCTION OF SYNGAS AND LIME BY COMBINED THERMO-NEUTRAL CALCINATION OF LIMESTONE WITH CO₂-REFORMING/PARTIAL OXIDATION OF METHANE OR CARBON

M. Halmann,^{a,*} and A. Steinfeld^b

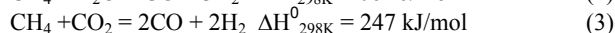
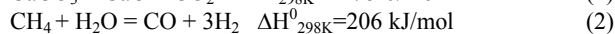
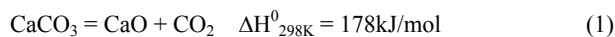
^a Weizmann Institute of Science, Department of Environmental Sciences and Energy Research, Rehovot 76100, Israel.

^b ETH - Swiss Federal Institute of Technology, Department of Mechanical and Process Engineering, CH-8092 Zurich, Switzerland.

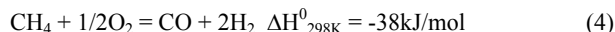
* Corresponding author. E-mail: m.halmann@weizmann.ac.il

Introduction

The calcination of limestone to produce lime and cement, as well as the steam/CO₂ reforming of natural gas, are highly energy-intensive processes, which together contribute more than 6% to the global anthropogenic CO₂ emissions,¹



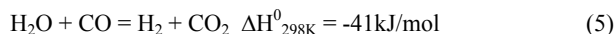
By combining these endothermic processes with the exothermal partial oxidation of methane,



it is possible to design overall thermo-neutral processes for the co-production of lime and the valuable syngas. In such a combination of the CO₂-emitting calcination with the CO₂-consuming reforming, most of the CO₂ release would be avoided. Also, the endothermicity of these processes would be compensated by the exothermicity of the CH₄ partial oxidation, resulting in fuel saving. The thermodynamic constraints for such combined processes were determined at 1200 and 1400 K. An analogous thermo-neutral co-production of metals and syngas has recently been developed.² Such combined processes, which both release CO₂ and utilize it, could be an attractive option for greenhouse gas mitigation.³

Results

The calculated equilibrium composition as a function of temperature from 800 to 1450 K for an initial reaction mixture of CaCO₃ – CH₄ – O₂ – H₂O is presented in Figure 1. As shown in the Figure, above 1100 K, CaO, H₂, and CO are stable reaction products. Equilibrium compositions for thermo-neutral reactions of CaCO₃ with O₂ and either CH₄ or carbon, in the absence and presence of added H₂O, are shown in Table 1. Carbon was taken for these calculations as a proxy of coal, which would be used in actual practice. The purpose of including H₂O in the reactant mixtures is to promote the *in situ* water-gas-shift reaction,



thus raising the H₂ to CO molar ratio to H₂/CO = 2, as required for the synthesis of methanol, which could be one of the useful products from syngas.

This preliminary assessment of the combined calcination of limestone with the partial oxidation of CH₄ or carbon predicts considerably decreased CO₂ emission, as well as competitive

economics, justifying further study.

References

1. Steinfeld, A.; Thompson, G., *Energy*, **1994**, 19, 1077-1081.
2. Halmann, M.; Frei, A.; Steinfeld, A. *Energy*, 2002, 27, 1069-1084.
3. Halmann, M. M.; Steinberg, M. *Greenhouse Gas Carbon Dioxide Mitigation: Science and Technology*, Lewis Publ., Boca Raton, **1999**.

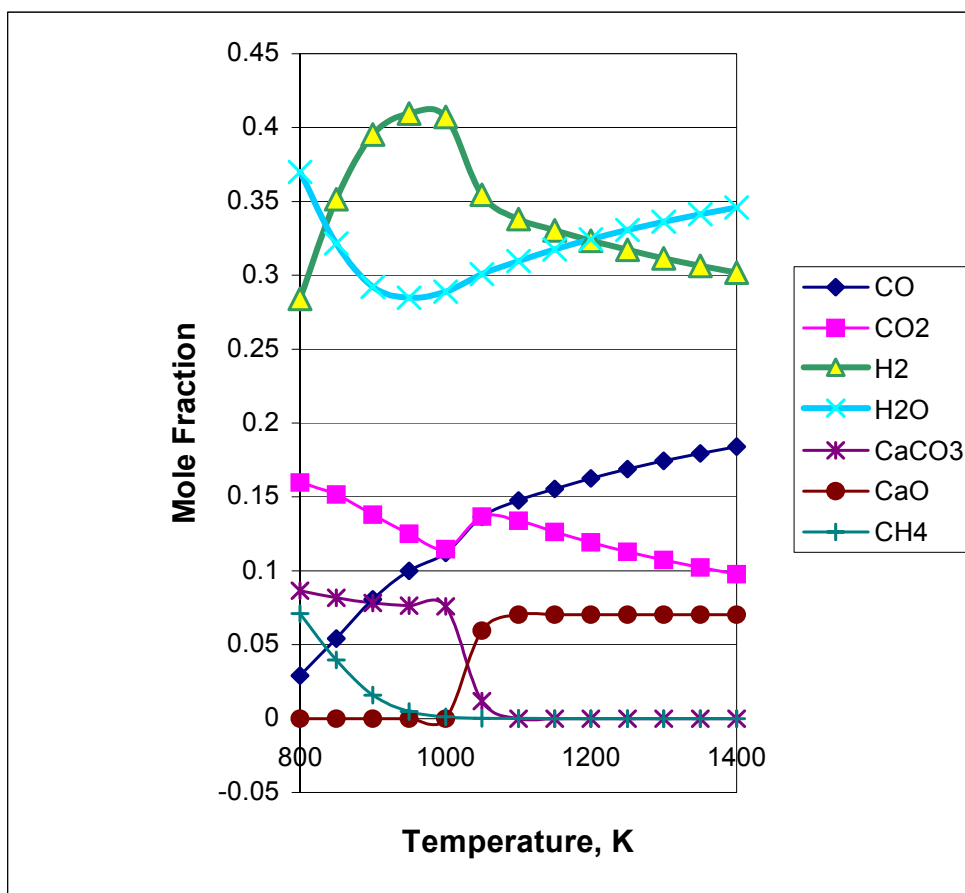


Figure 1. Equilibrium composition vs. temperature for $\text{CaCO}_3 - \text{CH}_4 - \text{O}_2 - \text{H}_2\text{O}$, initially with molar ratio 1 : 3 : 2.55 : 3.2 at 300 K and 1 bar.

Table 1. Computed equilibrium compositions for thermo-neutral reactions of CaCO_3 with O_2 and either CH_4 or carbon in the absence or presence of H_2O at 1200 K and 1 bar. Yields of H_2 are relative to the CH_4 input, while the CO yields are vs. the total carbon input ($\text{CaCO}_3 + \text{CH}_4$ or Carbon).

Initial mol	Initial mol	Initial O_2 mol	Initial H_2O mol	ΔH kJ/mol	H_2 Yield %	CO Yield %	H_2/CO molar ratio
CaCO_3 1.00	CH_4 2.00	1.80	-	-12.0	59.8	66.9	1.19
CaCO_3 1.00	CH_4 3.00	2.55	3.20	+11.7	76.5	57.7	1.99
CaCO_3 1.00	Carbon 2.00	1.20	-	-1.2	-	53.3	-
CaCO_3 1.00	Carbon 2.00	1.70	8.00	-5.2	5.0*	6.7	1.99

* H_2 yield calculated relative to H_2O input.

CATALYTIC PYROLYSIS AND KINETICS OF CORN STALK WITH THERMOGRAVIMETRY

Chuncai Song^a, Shengwei Zhu^a, Haoquan Hu^{a*}, Guohua Chen^b

^aInstitute of Coal Chemical Engineering, Dalian University of Technology, 129 Street, Dalian 116012, China

^bDepartment of Chemical Engineering, The Hong Kong University of Science & Technology, Clear Water Bay, Kowloon, Hong Kong SAR
*hhu@chem.dlut.edu.cn

Introduction

Recently, the global environmental problems, such as global warming and acid rain, have become a serious issue. Biomass, as a renewable and potential resource, its effective utilization has been received considerable attention worldwide. Biomass resources are abundant in China, but they are not been used efficiently, particularly in handling agricultural biomass that is often burned on site, causing not only environmental pollution but also waste of resource. Therefore, in China, it is of great significance to develop new technology to make rational and efficient use of biomass as an alternative energy for fossil fuels or to obtain chemicals.

Thermoanalytical techniques (TG and DTG) have been widely used to study the kinetics of various solid-state fossil fuels decomposition reactions. Researchers have proposed different models to study the characteristics of biomass pyrolysis in the past few years [1-3]. Distributed Activation Energy Model (DAEM), as a new and simple method, which is presented by Miura [4,5], has been used both in the cases where single reactions are occurring and analyzing complex reaction systems, such as pyrolysis of fossil fuels, thermal regeneration reactions of activated carbon and so on. Recently, Liu et. al. [6] gave the explicit analytic expression of activation energy during weight loss process based on the new theoretical analysis of DAEM. However, the application of DAEM to biomass pyrolysis has not been reported yet. It is especially necessary to understand the kinetics of pyrolysis in order to design a suitable pyrolysis reactor and obtain a better insight of effective catalyst or study the mechanisms of liquefaction or pyrolysis of biomass. In this paper, the pyrolysis of corn stalk with sodium carbonate or potassium carbonate as catalyst was carried out with thermal gravimetric analysis, and the activation energy distribution at different weight loss of biomass was determined with DAEM.

Experimental

Raw material Crushed and sieved air-dried biomass of corn stalk obtained from Dalian suburb, northeast of China, and the main components of biomass, including cellulose microcrystalline from Alfa Aesar, lignin with low sulfonate from Aldrich, hemicellulose, replaced with Poly(beta-D-xylopyranose) (xylan) from Sigma were used as the test samples in this study. A certain amounts of catalysts were dissolved in distilled water and impregnated test samples for two hours and then dried.

Equipment and method The pyrolysis of biomass was performed in a thermogravimetric analyzer (Mettler-Toledo TGA/SDTA851[®]). Approximately 6mg sample was placed in an Al₂O₃ ceramic pan. The furnace was heated from ambient temperature to 923K at a constant heating rate (5,10,20,40K/min). Purified nitrogen at a constant flow rate of 20mL/min was used as the purge gas to provide an inert atmosphere for pyrolysis and to remove any gaseous and condensable products evolved, thus minimizing any secondary vapor-phase interactions. The sample weight was recorded as a function of time or temperature.

Results and Discussion

Pyrolysis of corn stalk Figure.1 shows the TG and DTG curves of sodium carbonate and potassium carbonate at the heating rate of 10K/min during the pyrolysis. It can be seen that except about 2 to 3% weight loss of moisture before 420K there is no obviously weight loss with temperature further increased. Therefore, catalysts don't decompose in the range of temperature investigated in this work and the effect on the calculation of thermal gravity analysis in the following experiments can be eliminated by subtracting the quantities of catalyst according to the amount added in the sample.

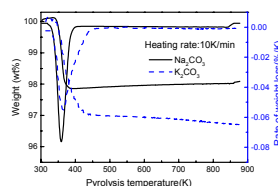


Figure 1. TG and DTG curves of sodium and potassium carbonate

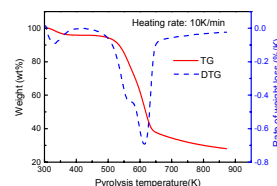


Figure 2. TG and DTG curves of corn stalk

Figure 2 shows TG and DTG curves of corn stalk without any catalyst. It can be observed that the main pyrolysis region of corn stalk is between about 500K and 650K. There are two peaks at 572K and 614K in the DTG curve correspondingly and a long tail at high temperatures. Compared to the TG and DTG curves of hemicellulose, cellulose and lignin shown in Figure 3, the first peak on DTG curve of corn stalk is mainly contributed by hemicellulose, the second one by cellulose and the long tail corresponds to the thermal decomposition of lignin.

Figure 4 and Figure 5 show the catalytic effect on the TG and DTG curves with Na₂CO₃ and K₂CO₃ (0.5, 1.0, 3.0 and 10wt%) addition, respectively. Compared with the result without catalyst addition, catalyst has an effect on pyrolysis of biomass at temperature after about 470K, especially in the range of 550K to 650K. Catalyst can increase the final weight loss of corn stalk. Without catalyst the weight loss is 62.4wt%, while 69.9wt% with addition of 1wt% Na₂CO₃ and 73.1wt% with 1wt% K₂CO₃. But when K₂CO₃ addition is more than 3.0wt%, the final weight loss decreased by about 4wt%, see Fig.5 (A). For the case of Na₂CO₃, more catalyst added, the lower temperature at the maximum weight loss rate results in, from 620K with 0.5wt% to 565K with 10wt% Na₂CO₃. Generally speaking, when catalyst addition is more than 1.0wt%, the shape of the curve of DTG is greatly changed, from two peaks to only one peak meaning that catalyst has more effect on hemicellulose than that on the other main fractions of biomass.

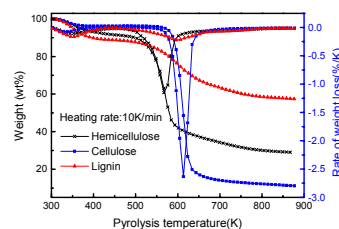


Figure 3. TG and DTG curves of hemicellulose, cellulose and lignin

Figure 6 shows the DTG curves for corn stalk with 3.0wt% Na₂CO₃ or K₂CO₃ and without addition of catalysts at heating rate of 20K/min. Both catalysts can increase the maximum weight loss rate and have obvious effect on pyrolysis results. Under this condition, the temperature at the maximum weight loss rate is 604K with K₂CO₃ and 607K with Na₂CO₃.

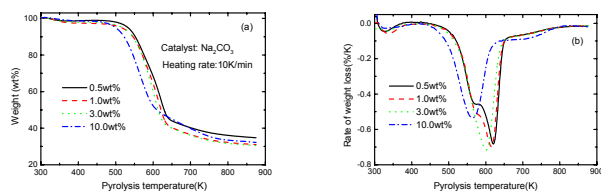


Figure 4. TG and DTG curves of corn stalk with different amounts of sodium carbonate addition (A) TG; (B) DTG

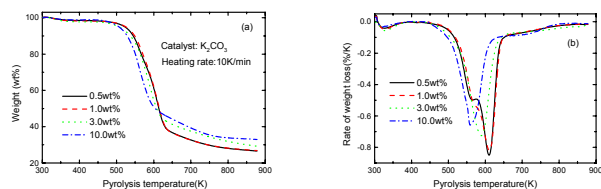


Figure 5. TG and DTG curves of corn stalk with different amounts of potassium carbonate addition (A) TG; (B) DTG

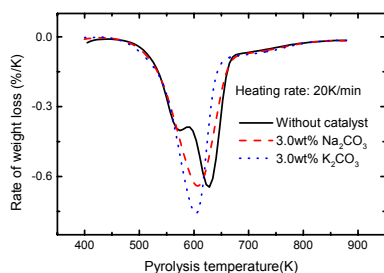


Figure 6. Comparison of DTG curves with different catalyst

Determination of activation energy with DAEM DAEM is based on the following assumptions: 1) complex reactions are consisted of a series of irreversible first-order reactions that have different activation energies and a constant frequency factor. That is, all the reactions are parallel; 2) All the activation energies present continuous distribution functional forms. When applied to pyrolysis, DAEM is expressed as:

$$\frac{\omega}{\omega_0} = 1 - \int_0^\infty \Phi(E, T) f(E) dE \quad (1)$$

where ω is the total volatile matter evolved by time t , ω_0 is the effective volatile matter content of the raw material, $f(E)$ is the distribution function of activation energy to represent the differences in the activation energies of many first-order irreversible reactions.

The $\Phi(E, T)$ function is equal to

$$\Phi(E, T) = \exp\left(-\frac{k_0 RT^2}{hE} e^{-E/RT}\right) \quad (2)$$

and k_0 is the frequency factor corresponding to E value, h is heating rate; R is 8.314(J/mol K). Eq (1) is the function of temperature T and heating rate h . Therefore, at a constant heating rate h , ω/ω_0 satisfies:

$$d(\omega/\omega_0) = \frac{\partial(\omega/\omega_0)}{\partial T} dT + \frac{\partial(\omega/\omega_0)}{\partial h} dh = 0 \quad (3)$$

from eq(1) to eq(3), following equation can be deduced^[6].

$$\frac{E}{R} = -\frac{d \ln h}{d(1/T)} - 2T \quad (4)$$

Using eq (4), $f(E)$ and k_0 can be estimated from TG data obtained at

different heating rates^[6].

Since at temperature below 423K mainly weight loss is due to dehydration, we set the weight loss of samples as 0wt% at the temperature 423K, while 100wt% at the final pyrolysis temperature. That is: $\alpha = 1 - \omega/\omega_0$, where α is weight loss fraction; ω and ω_0 are the same nomenclatures as above.

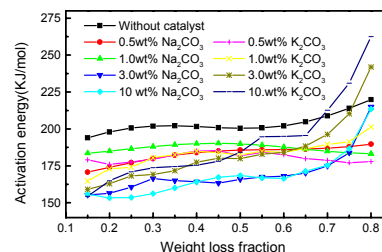


Figure 7. Activation energy vs weight loss obtained by DAEM

Figure 7 gives the activation energy obtained by DAEM based on eq (4) for different samples. It can be seen that activation energy of corn stalk is between 194 and 220kJ/mol in the weight loss range of 15% to 80%. And it is interesting that activation energy value, varying continuously with the increasing of temperature, indicated that the thermal pyrolysis of corn stalk is not a single reaction, but a complex reaction containing a series of cracking of chemical bonds with different activation energies. Generally activated energy can be reduced by about 20–40 KJ/mol owing to the addition of catalyst. Sodium carbonate and potassium carbonate are both effective and potential catalyst for biomass conversions.

Conclusions

The results indicated that the catalyst has an effect about upon 470K, especially in the range of 550K~650K. When catalyst addition is more than 1.0wt%, DTG curve is altered greatly, from two peaks to one, for catalyst affecting more on hemicellulose than on cellulose and lignin. In the case of Na_2CO_3 , the more added, the lower the temperature at maximum weight loss rate, from 620K with 0.5wt% to 565K with 10wt%.

The DAEM analysis shows that the activation energy is between 194 and 220kJ/mol in the weight loss range of 15% to 80%, which indicated that corn stalk pyrolysis is a complex reaction containing a series of cracking of chemical bonds with different activation energies. Catalyst can reduce activation energies by about 20 to 40 KJ/mol depending on the added amounts.

Acknowledgment

The authors are grateful for financial support by the Special Research Foundation for Doctoral Education of China (No. 2000014115).

References

- [1] Demirbas, A. *Bioresource Technology*, 1998, 66, 247.
- [2] Kim, S.; Park, J. K. *Thermochimica Acta*, 1995, 264, 137.
- [3] Guo, J.; Lua, A. C. *Biomass and Bioenergy*, 2001, 20, 223.
- [4] Miura, K. *Energy & Fuels*, 1995, 9, 302.
- [5] Miura, K.; Maki, T. *Energy & Fuels*, 1998, 12, 864.
- [6] Liu, X.G.; Li, B.Q.; Miura, K. *Fuel Processing Technology*, 2001, 69, 1.

PREDICTION OF THE REID VAPOR PRESSURE OF PETROLEUM FUELS

M. R. Riazi*, T. A. Albahri and A. H. AlQattan

Chemical Engineering Department, Kuwait University,
P.O.Box 5969, Safat 13060, Kuwait

*Tel: (+965) 4817662; Fax: (+965) 4811772

*Homepage: <http://139.141.199.1/~riazi>

riazi@kuc01.kuniv.edu.kw

Introduction

The volatility characteristics of petroleum fuels are very important especially for gasolines. Motor and aviation gasolines are manufactured as liquids but they are consumed in the vapor phase. Consequently, gasoline volatility must be high enough to assure acceptable engine start-up, warm-up, acceleration and throttle-response under normal driving (or flying) conditions. On the other hand, the maximum volatility of a gasoline must be restricted to avoid vapor lock, vaporization losses, air pollution, and unsafe storage and handling. The volatility considerations for other transportation fuels like kerosene and diesel are, to some extent, similar to those for gasoline.

The Reid vapor pressure (RVP) is frequently used as an indication of volatility of liquid hydrocarbons. The RVP is defined as the absolute pressure (i.e., psia or bar) exerted by a mixture, determined at 100 °F (37.8 °C) and at a vapor to liquid ratio of 4. This is different than the true vapor pressure which is defined as the pressure of a vapor in equilibrium with its condensed phase at a specific temperature. Although the RVP provides a convenient approximation of the absolute vapor pressure of a partly vaporized sample at 100 °F, it is not equivalent to the true vapor pressure. In general, RVP is lower than the true vapor pressure due to some small sample vaporization and the presence of water vapor and air in the confined space. The apparatus and procedures for determining the RVP are standardized and specified in ASTM method D-323 and IP-402 [1]. The Reid vapor pressure test is widely used as a criterion for blending gasoline and other petroleum products. Once RVP of a fuel is known the methods provided in the API-TDB [2] can be used to estimate true vapor pressure of a fuel or a crude oil at any desired temperature. True vapor pressure is an important thermodynamic property related to volatility and phase equilibrium calculations.

There are a number of methods for estimating the vapor pressure of petroleum fractions but very few for Reid vapor pressure. The method presented in the API-TDB [2] for estimation of RVP is based on rigorous vapor-liquid equilibrium calculations. A number of simple methods have been developed to estimate the Reid vapor pressure of finished petroleum products [3]. In the Bird-Kimball method the gasoline is divided into 28 cuts or boiling ranges characterized by their average boiling point. A blending RVP of each cut is then calculated by the following equation [3]:

$$B_i = \frac{7.641}{\exp(0.03402 T_{bi} + 0.6048)} \quad (1)$$

$$P_a = \sum_{i=1}^{i=28} B_i x_{vi}$$

$$f = 1.0 + 0.003744 (\text{VAPB} - 93.3)$$

$$\text{RVP} = f P_a$$

where B_i = RVP blending number for cut i and T_{bi} = normal boiling point of cut i in °C. x_{vi} is the volume fraction of cut i and VABP is the volume average boiling point in °C. RVP is calculated in bars. The constants were obtained from the original constants given in

English units. Use of this method requires full distillation curve of the fuel to be known. Another simple method is to use a relation for the true vapor pressure (TVP) of petroleum fractions and to assume that RVP is the same as TVP at 100 °F (311 K). The vapor pressure relation given by van Nes van Westen [4] can be converted into the SI unit at 311 K as:

$$\log(\text{TVP})_{100} = 3.204 \times \left(1 - 4 \times \frac{T_b - 41}{1393 - T_b} \right) \quad (2)$$

where T_b is the normal boiling point in K and TVP_{100} is the true vapor pressure at 100 °F (311 K) in bars. Once TVP is calculated it may be used instead of RVP in case of lack of sufficient data. This method only requires mid-boiling point (or ASTM temperature at 50 volume% vaporized). This gives an approximate value for RVP as the difference between RVP and TVP is ignored. The main objective of this work was to develop a simple predictive method for RVP of petroleum fuels from crude oils from around the world which requires minimum laboratory data as input parameters.

Technical Development

A bank of data on RVP and basic characteristics of 52 gasoline and naphtha samples from crude oils around the world was prepared from OGJ Data Book [5]. One simple and relatively accurate equation for correlation of true vapor pressure of hydrocarbons is the Miller equation [6]. We apply this equation at 311 K (100 °F), however, the constants in the equation have been determined from RVP of petroleum fractions and have been related to boiling point (T_b) and specific gravity (SG) of the fraction in the following form:

$$\text{RVP} = P_c \exp(Y)$$

$$Y = -X \left(\frac{T_b \text{SG}}{T_r} \right) (1 - T_r)^5 \quad (3)$$

$$X = -276.7445 + 0.06444 T_b + 10.0245 \text{SG} - 0.129 T_b \text{SG}$$

$$+ \frac{9968.8675}{T_b \text{SG}} + 44.6778 \ln T_b + 63.6683 \ln \text{SG}$$

$$T_r = 311/T_c$$

where T_c and P_c are the pseudocritical temperature and pressure of the fraction in degrees Kelvin and bar, respectively. RVP is in bars and T_b mid-boiling point of mixture in degrees Kelvin. This equation is based on data with RVP in the range of 0.0007-1.207 bar (0.01 – 17.5 psia), normal boiling point range of 305 – 494 K and specific gravity range of 0.65-1.08. This method may be used for quick estimation of RVP when only boiling point and specific gravity of a fuel are known. This equation does not give reliable values for RVP of wide boiling range fractions such as the whole crude oil. T_c and P_c needed for use in the above equation may be estimated from the relations given by Riazi and Daubert [7] that are also included in the API-TDB [2] using T_b and SG as input parameters. Therefore, with the minimum knowledge of mid-boiling point and specific gravity one can get estimate of RVP from Equation (3). A summary of evaluation of these three methods is given in Table 1. Equations (1) and (2) nearly give similar result, although Equation (2) is much simpler than Equation (1). However, the average error for Equation (3) is 0.06 bar (0.88 psia) which is nearly half of the other two methods. Predicted versus experimental values of RVP from the

proposed method is also shown in Figure 1. Demonstrated results indicate that when minimum data on a petroleum fuel is available the method proposed in this work can be used to estimate RVP of a fuel.

Table 1. Summary of Results for Prediction of RVP of 52 Fuels

Item	Method	Eqn.	RVP (bar)	
			AAD	MD
1	Proposed model	3	0.06	0.24
2	Nes and Van Westen [4]	2	0.13	0.38
3	Bird and Kimball [3]	1	0.12	0.42

API Gravity range: 51 – 87 °API, T_b Range: 305 – 494 K

RVP Range: 0.0007-1.207 bar,

AAD% = $(1/\text{no of data}) \sum |(\text{pred.} - \text{exp.})/\text{exp.}| \times 100$,

MD%= maximum % deviation

References

- (1) ASTM, "Annual Book of Standards," American Society for Testing and Materials, Philadelphia, Pennsylvania, 1995.
- (2) American Petroleum Institute (API) Technical Data Book – Petroleum Refining. Chapter 5, 6th Edition, American Petroleum Institute., Washington DC, 1997.
- (3) Baird, C.T. Crude Oil Yields and Product Properties, Ch. De la Haute Belotte 6, 1222 Vezenaz, Geneva, Switzerland, 1981.
- (4) Van Nes, K., and Van Western, H.A., Aspects of the Constitution of Minerals Oils, Elsevier, Amsterdam, 1951.
- (5) Oil and Gas Journal Data Book, 2000 Edition, PennWell, Tulsa, Oklahoma, 2000.
- (6) Reid, R. C., Pransnitz, J. W., and Poling, B. E. The Properties of Gases and Liquids. 4th Edition., McGraw-Hill, Inc., New York, 1987.
- (7) Riazi, M.R., Daubert, T.E., "Characterization Parameters for Petroleum Fractions," Ind. & Eng. Chem. Research, 1987, Vol. 26, pp. 755-759.

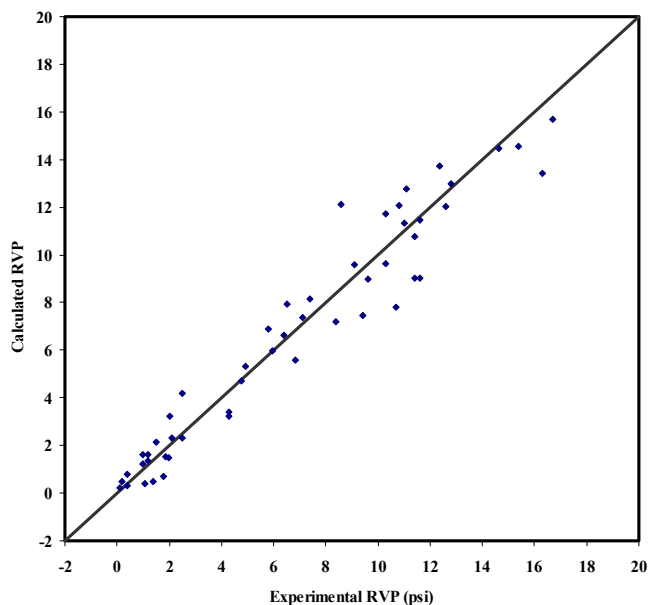


Figure 1. Parity plot for the Reid vapor pressure (RVP) using Equation (3).